Monthly Notices of the ROYAL ASTRONOMICAL SOCIETY
MNRAS **553,** 1–17 (2026) https://doi.org/10.1093/mnras/stag1788

A proto-brown dwarf candidate ejected from a multiple system and hosting a highly substructured disc

Ricardo Hernández-Garnica [1★], Aina Palau [1★], Laurent Loinard [1,2], Dimitris Stamatellos [3], Matthew Teasdale [3], Ernesto Becerra-Aguirre [1], Aníbal E. Sierra [4], Jesús A. Toalá [1], María J. Maureira [5], Nuria Huélamo [6], Diego A. Vasquez-Torres [1], Carlos Carrasco-González [1], Raúl F. Maldonado [1] and Carlos G. Román-Zúñiga [7]

[1]*Universidad Nacional Autónoma de México, Instituto de Radioastronomía y Astrofísica, Antigua Carretera a Pátzcuaro 8701, Ex-Hda. San José de la Huerta, 58089 Morelia, Michoacán, México*
[2]*Black Hole Initiative at Harvard University, 20 Garden Street, Cambridge, MA 02138, USA*
[3]*Jeremiah Horrocks Institute for Mathematics, Physics and Astronomy, University of Lancashire, Preston PR1 2HE, UK*
[4]*Universidad Nacional Autónoma de México, Instituto de Astronomía. A.P. 70-264, 04510 Ciudad de México, México*
[5]*Max-Planck-Institut für extraterrestrische Physik (MPE), Gießenbachstr. 1, D-85741 Garching, Germany*
[6]*Centro de Astrobiología (CAB), CSIC-INTA, ESAC Campus, Camino bajo del Castillo s/n, E-28692 Villanueva de la Cañada, Madrid, Spain*
[7]*Universidad Nacional Autónoma de México, Instituto de Astronomía. A.P. 106, 22800 Ensenada, B.C., México*

Accepted 2026 September 11. Received 2026 September 11; in original form 2026 February 16

ABSTRACT

Disc fragmentation and subsequent ejection after a dynamical interaction is a potential formation mechanism of brown dwarfs (BDs). However, the number of BDs with robust evidence of being ejected is very scarce. Using multi-epoch observations obtained with the ALMA and VLA interferometers, we present an astrometric study of the proper motions of two very low luminosity objects located north-east of the VLA 1623 system: SM1-A and the proto-brown dwarf candidate called Source X. The astrometric study suggests that Source X is moving at ~ 4 km s^{-1} relative to VLA 1623 B and might have been ejected from the nearby multiple system VLA 1623 about 3000–7000 yr ago. What is more, the disc of Source X is well resolved at both 1 mm and 3 mm, and presents a prominent, massive, optically thick ring-like structure whose properties are not typical of protoplanetary discs. The disc fragmentation scenario around a single and a binary object is explored with numerical simulations. This scenario can produce close ejected proto-BD binaries retaining their circumbinary discs, although the discs around the ejected objects are more compact and less massive than the one observed in Source X. Overall, Source X stands out as a promising proto-BD candidate ejected from a multiple system, and whose disc properties call for further research on numerical modelling of discs around ejected very low-mass objects.

Key words: brown dwarfs – proper motions – astrometry – stars: protostars – protoplanetary discs – star formation.

1 INTRODUCTION

Brown dwarfs (BD) and free-floating planets (FFPs) have attracted attention since their discovery in the mid-nineties, because their existence challenges the formation mechanisms currently accepted for stellar objects, and might be linked to the formation of planets. BDs are objects whose mass is not large enough to undergo persistent nuclear fusion of hydrogen in their interiors, and have masses $\lesssim 0.075$ M$_\odot$. FFPs, or isolated planetary-mass objects, are assumed to have masses $\lesssim 0.010$ M$_\odot$ (see discussion in A. Palau et al. 2024). The formation of these very low-mass objects is a matter of intense debate. One possibility is that they form as a scaled-down version of low-mass stars, that is, as a product of fragmentation of molecular clouds (see e.g. A. Palau et al. 2024; A. A. Ahmad et al. 2025, and references therein). In this case, it would be expected that the initial mass function (IMF) follows approximately a specific parametrization or power-law in the low-mass end (e.g. G. Chabrier 2005; P. Kroupa et al. 2013; T. Haugbølle, P. Padoan & Å. Nordlund 2018; M. R. Bate 2019; G. Chabrier & R. Lenoble 2023).

However, recent works have shown that, in certain clouds of the Solar neighbourhood, there is an excess of substellar objects with respect to the expected IMF, suggesting that additional mechanisms could be at work (e.g. N. Miret-Roig et al. 2022). In addition, the observations of binary separation distributions and binary mass ratios of stars and BDs in the field (e.g. H. Bouy et al. 2003; A. J. Burgasser et al. 2003; L. M. Close et al. 2003) do not seem to match the expected theoretical predictions (e.g. I. Thies et al. 2015) and seem to be more aligned with a dynamical origin, for which tight separations and near-equal masses are

★ E-mail: r.hernandezg@irya.unam.mx (RH); a.palau@irya.unam.mx (AP)

© The Author(s) 2026.
Published by Oxford University Press on behalf of Royal Astronomical Society. This is an Open Access article distributed under the terms of the Creative Commons Attribution License (https://creativecommons.org/licenses/by/4.0/), which permits unrestricted reuse, distribution, and reproduction in any medium, provided the original work is properly cited.

Downloaded from academic.oup.com/mnras/article/553/1/stag1788/9006207 by guest on 09 November 2026

expected (e.g. B. Reipurth & S. Mikkola 2015). As a consequence, an alternate scenario that naturally explains the aforementioned observations involves a dynamical origin of BDs and FFPs.

Models considering dynamical events can be grouped into two main categories. First, there is a group of models that consider a dynamical interaction between stellar embryos or protostellar cores (e.g. B. Reipurth & C. Clarke 2001; P. Kroupa & J. Bouvier 2003). In these models, a molecular cloud is undergoing fragmentation (e.g. following the Jeans criterion), and the resulting objects undergo dynamical interactions and ejections, halting their subsequent accretion (e.g. M. R. Bate & I. A. Bonnell 2005). Indirect evidence of this scenario is based on the spatial distribution of substellar objects or their velocity dispersions (e.g. M. S. N. Kumar & S. Schmeja 2007; S. Boudreault & C. A. L. Bailer-Jones 2009), although whether the ejected objects should present significant kinematic differences with respect to the objects formed *in situ* is a matter of debate (e.g. P. Kroupa & J. Bouvier 2003; M. R. Bate 2009).

The second group of models involving dynamical interactions for BD and FFP formation considers that the dynamical interaction takes place among the objects formed in a protostellar disc. These objects could have formed through disc fragmentation (e.g. D. Stamatellos, D. A. Hubber & A. P. Whitworth 2007a; D. Stamatellos & A. P. Whitworth 2009; O. Schib et al. 2025) or core accretion and planet–planet scattering (e.g. H. G. Bhaskar & H. B. Perets 2025; K. Guo, S. Ida & M. Ogihara 2026). The process has also been recently explored for the case of ejection of Jupiter-mass objects from accreting binary systems (A. Ćalović et al. 2026). It is important to note that, in this scenario, the ejected velocities are expected to be low and barely distinguishable from the field stars (D. Stamatellos & A. P. Whitworth 2009; H. G. Bhaskar & H. B. Perets 2025; S. Hadden & Y. Wu 2026). If this scenario is at work and if the ejected objects were formed through core accretion, it would be expected that the ejected objects present super-solar metallicities, mainly because only the refractory material survives near the host star and migration processes favour metal-rich planetesimal accretion (e.g. N. Madhusudhan et al. 2016).

Thus, the aforementioned predictions and evidence that could potentially favour dynamical scenarios are all indirect, and the confirmed number of BDs or FFPs found to be ejected in dynamical interactions of protostellar cores or from multiple systems is very small. For example, E. Akiyama et al. (2019) present the case of a protoplanetary disc displaying a long tail and suggest it could result from a dynamical interaction. More recently, S. Dong et al. (2026) report the detection of a microlensing event, produced by a Saturn-mass object that corresponds to an FFP at 3 kpc from the Sun. These authors infer, indirectly (that is, from statistical arguments and comparison with numerical simulations), that the FFP must have been ejected from a protoplanetary disc. In spite of these efforts focused on individual objects, there is still no direct evidence in favour of the dynamical ejection scenario.

Definite examples of BDs or FFPs should show that the ejected objects actually come from a specific ejection site, and this could be explored through precise astrometry. This approach was taken by A. K. P. Yip et al. (2023), who used the Tycho-Gaia astrometric solution to identify one promising ultra-cool dwarf most likely resulting from a dynamical interaction. One of the most convincing examples of an ejected object is presented by B. Reipurth et al. (2023), who suggest that a very low mass star, H α5, was ejected at 25 km s^{-1} from the multiple system associated with HH24, about 5800 yr ago (see fig. 35 of B. Reipurth et al. 2023). As further examples of ejected objects are found, it will be possible to assess the relevance of this mechanism for BD and FFP formation.

In this work, we present a study of the proper motions of the very low-mass objects Source X and SM1-A (R. Kawabe et al. 2018; A. Palau et al. 2024) near the multiple system VLA 1623 located in the Ophiuchus cloud at 137.3 pc of distance (G. N. Ortiz-León et al. 2017). Fig. 1 shows a *James Webb Space Telescope* (*JWST*) image in colourscale, with an Atacama Large Millimeter/submillimeter Array (ALMA) image superimposed in contours, covering the multiple system VLA 1623 along with Source X and SM1-A (F. Nakamura et al. 2025). The figure includes the VLA 1623 system (A + B, W) to the southwest, Source X near the centre at about $\sim$ 20 arcsec to the northeast of VLA 1623, and SM1-A $\sim$ 20 arcsec to the north of Source X. Since VLA 1623 harbours a multiple system of at least 4 objects (Aa, Ab, B, and W), it could be a potential site of dynamical interaction of protostellar cores, as in the case of HH24 reported by B. Reipurth et al. (2023). In addition, the VLA 1623 system had been previously considered as a potential site of disc fragmentation and subsequent ejection (e.g. R. J. Harris et al. 2018), with VLA 1623 W potentially ejected from the triple A + B system. More recent works (e.g. S. I. Sadavoy et al. 2024; R. Hernández-Garnica et al. 2026) conclude that this is an unlikely possibility for VLA 1623 W. Still, given the high order of the VLA 1623 multiple system, the area surrounding this system is an excellent place to search for objects potentially ejected from it, either by a dynamical interaction among the individual members of the system, or from the discs associated with one of the members.

This paper is organized as follows. In Section 2, the compilation of ALMA and VLA observations used to study the proper motions is presented. Section 3 gives the main results of this study, revealing an anomalous proper motion and a peculiar disc for Source X. In Section 4, the possible ejection from the VLA 1623 system is compared to the outcome of numerical simulations of the disc fragmentation scenario. Finally, in Section 5 we discuss the nature of Source X and the possible origin of its substructured disc.

2 OBSERVATIONS

The observations included in this work were collected with ALMA and the Very Large Array (VLA), and were obtained from the ALMA and NRAO archives, respectively. We included a total of 5 VLA and 12 ALMA observations obtained between 2012.50 and 2023.62 for SM1-A, and between 2015.33 and 2023.62 for Source X. This corresponds to a time span of approximately 11 and 8 yr for SM1-A and Source X, respectively. The ALMA data were recorded in bands 3 (84–116 GHz), 4 (125–163 GHz), 5 (163–211 GHz), 6 (211–275 GHz), and 7 (275–373 GHz). The VLA observations were conducted in bands X (10 GHz), K (22 GHz), and Q (45 GHz). All 17 observations are listed in Table 1, where the observing dates and corresponding frequency bands are provided.

All VLA data were obtained after the upgrade described by R. A. Perley et al. (2011), and calibrated using the VLA Pipeline version 2022.2.0.64, as part of the CASA software package (Common Astronomy Software Applications; J. McMullin et al. 2007), version 6.4.1. On the other hand, the ALMA data were reduced using different versions of CASA and the ALMA pipeline, as specified in the QA2 reports available in the ALMA archive for each corresponding project. All images were made using the CASA task tclean, whose imaging parameters are indicated in Table 1. In

Downloaded from academic.oup.com/mnras/article/553/1/stag1788/9006207 by guest on 09 November 2026

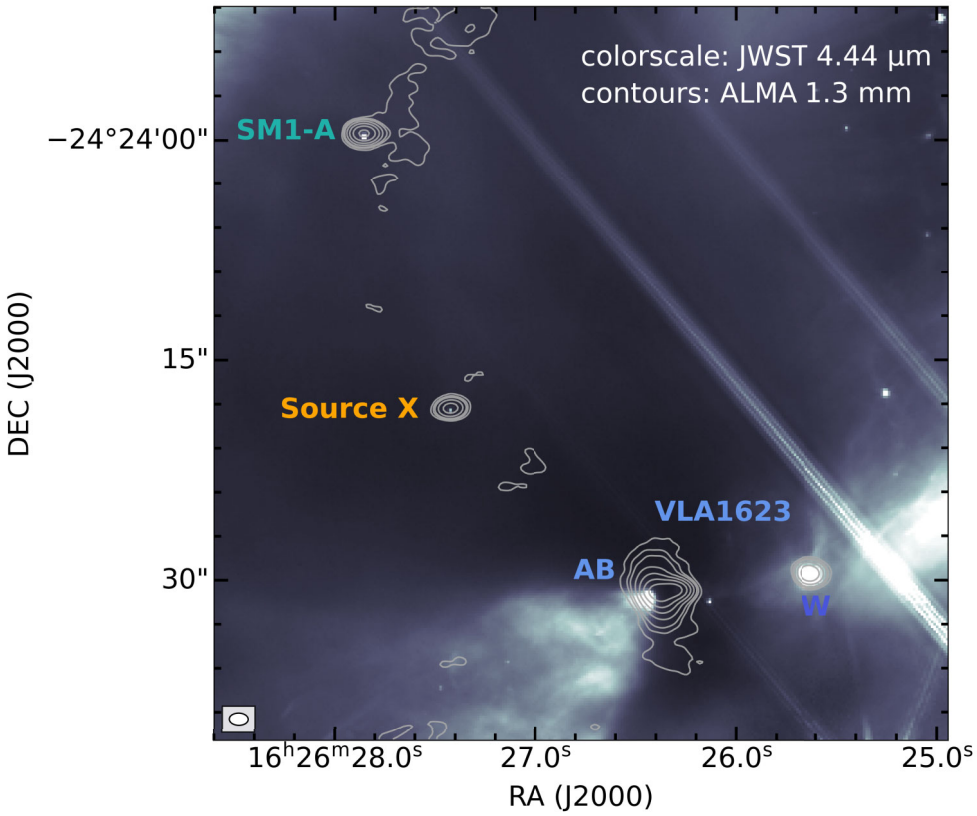


Figure 1. ALMA 1.3 mm emission (in contours, F. Nakamura et al. 2025) overlaid on the *JWST* 4.44 μm image (colour scale) of the VLA 1623 multiple system, Source X, and SM1-A. Contours correspond to levels 4, 8, 12, 24, 48, 96, and 192 times the rms of the image, 0.5 mJy beam^{-1}. The ALMA synthesized beam, of 1.28 × 0.83 arcsec^2 and position angle 88.8°, is shown in the bottom-left corner. The VLA 1623 multiple system, Source X, and SM1-A are detected in both the ALMA and *JWST* images.

Table 1. List of VLA and ALMA observations of Source X and SM1-A.

Index	Date	Band	Gain calibrator (J2000)	Project	Beam size (arcsec^2; °)	Noise (mJy/beam)	Robust
01	2012.50	Q	1625-2527	12A-260	0.30×0.12; +08.27	0.04	+ 0.5
02	2012.63	7	1626-298	2011.0.00396.S	0.54×0.39; −78.17	1.45	+ 0.5
03	2015.33	6	1625-2527	2013.1.00839.S	1.28×0.83; +88.84	0.35	+ 0.5
04[a]	2015.39	6	1625-2527	2013.1.00937.S	0.56×0.27; +125.90	0.07	+ 0.5
05	2016.84	X	1625-2527	16B-259	0.59×0.21; +30.76	0.01	+ 2.0
06	2016.93	X	1625-2527	16B-259	0.76×0.23; +39.09	0.01	+ 2.0
07	2017.04	X	1625-2527	16B-259	0.57×0.22; +30.72	0.01	+ 2.0
08	2017.34	3	1625-2527	2016.1.01468.S	0.83×0.68; −75.00	0.16	+ 0.5
09	2017.38	6	1625-2527	2015.1.01112.S	0.34×0.30; +83.38	0.25	+ 2.0
10	2017.53	6	1625-2527	2015.1.01112.S	0.25×0.14; −78.06	0.32	+ 2.0
11	2019.73	3	1626-2951	2018.1.01205.L	0.52×0.30; −79.01	0.06	+ 0.5
12	2021.60	6	1633-2557	2019.1.01074.S	0.06×0.05; +68.71	0.03	+ 0.5
13	2021.68	3	1633-2557	2019.1.01074.S	0.09×0.06; −75.95	0.01	+ 2.0
14	2022.26	K	1625-2527	22A-164	0.19×0.09; −00.26	0.01	+ 2.0
15	2022.55	4	1617-2537	2018.1.00769.S	0.29×0.19; −89.66	0.05	+ 0.5
16	2022.61	5	1617-2537	2018.1.00769.S	0.34×0.27; +88.95	0.32	+ 0.5
17	2023.62	3	1617-2537	2022.1.01734.S	0.09×0.06; +85.60	0.03	+ 2.0

Note. [a] The beam size, noise, and Robust weighting information for the image from project 2013.1.00937.S were taken from R. K. Friesen et al. (2018).

Downloaded from academic.oup.com/mnras/article/553/1/stag1788/9006207 by guest on 09 November 2026

Table 2. Positions for Source X and SM1-A are listed prior to any astrometric correction, following the correction to the gain calibrator's catalogued position, and after applying both the gain calibrator position correction and the parallax correction. The uncertainties reported in the final two columns include systematic errors derived from the fitting procedures (see text).

			Before any corrections		After gain calibrator correction		After parallax correction	
Date	Band	Source	RA (J2000)	Dec. (J2000)	RA (J2000)	Dec. (J2000)	RA (J2000)	Dec. (J2000)
			^{s} from 16^h26^m	arcsec from $-24^\circ23'$	^{s} from 16^h26^m	arcsec from $-24^\circ23'$	^{s} from 16^h26^m	arcsec from $-24^\circ23'$
2012.50	*Q*	SM1A	27.8586	59.4693	27.8585	59.4693	27.8588 ± 0.0013	59.4696 ± 0.0103
2012.63	7	SM1A	27.8571	59.4907	27.8579	59.4907	27.8584 ± 0.0013	59.4918 ± 0.0112
2015.33	6	SM1A	27.8542	59.5550	27.8542	59.5550	27.8539 ± 0.0013	59.5542 ± 0.0112
2015.39[a]	6	SM1A	27.8560	59.5700	27.8560	59.5700	27.8559 ± 0.0014	59.5695 ± 0.0123
2016.84	*X*	SM1A	27.8600	59.5020	27.8599	59.5020	27.8602 ± 0.0033	59.5028 ± 0.0553
2016.93	*X*	SM1A	27.8556	59.5581	27.8556	59.5581	27.8556 ± 0.0033	59.5584 ± 0.0552
2017.04	*X*	SM1A	27.8556	59.5769	27.8556	59.5769	27.8552 ± 0.0033	59.5764 ± 0.0553
2017.34	3	SM1A	27.8556	59.5834	27.8556	59.5834	27.8554 ± 0.0013	59.5826 ± 0.0112
2019.73	3	SM1A	27.8522	59.6664	27.8522	59.6662	27.8527 ± 0.0013	59.6674 ± 0.0112
2021.68	3	SM1A	27.8528	59.7102	27.8528	59.7094	27.8533 ± 0.0013	59.7106 ± 0.0113
2022.26	*K*	SM1A	27.8505	59.7268	27.8505	59.7268	27.8501 ± 0.0013	59.7257 ± 0.0092
2023.62	3	SM1A	27.8508	59.7675	27.8508	59.7676	27.8513 ± 0.0013	59.7686 ± 0.0118
			^{s} from 16^h26^m	arcsec from $-24^\circ24'$	^{s} from 16^h26^m	arcsec from $-24^\circ24'$	^{s} from 16^h26^m	arcsec from $-24^\circ24'$
2015.33	6	Source X	27.4248	18.2984	27.4248	18.2984	27.4245 ± 0.0018	18.2975 ± 0.0220
2015.39[a]	6	Source X	27.4280	18.3170	27.4280	18.3170	27.4279 ± 0.0019	18.3165 ± 0.0226
2017.34	3	Source X	27.4283	18.3312	27.4283	18.3312	27.4280 ± 0.0018	18.3305 ± 0.0220
2017.38	6	Source X	27.4225	18.2892	27.4225	18.2892	27.4224 ± 0.0018	18.2887 ± 0.0221
2017.53	6	Source X	27.4233	18.2961	27.4233	18.2961	27.4236 ± 0.0018	18.2966 ± 0.0220
2019.73	3	Source X	27.4234	18.3812	27.4234	18.3809	27.4239 ± 0.0018	18.3821 ± 0.0220
2021.60	6	Source X	27.4236	18.4105	27.4237	18.4097	27.4242 ± 0.0018	18.4106 ± 0.0232
2021.68	3	Source X	27.4248	18.4324	27.4248	18.4316	27.4253 ± 0.0018	18.4328 ± 0.0220
2022.55	4	Source X	27.4245	18.4602	27.4245	18.4603	27.4249 ± 0.0019	18.4610 ± 0.0232
2022.61	5	Source X	27.4254	18.4496	27.4254	18.4497	27.4259 ± 0.0018	18.4506 ± 0.0223
2023.62	3	Source X	27.4242	18.4707	27.4242	18.4708	27.4247 ± 0.0018	18.4718 ± 0.0220

Note. [a] For the observation carried out in 2015.39, corresponding to project 2013.1.00937.S, the positions in right ascension and declination prior to any corrections were taken from R. K. Friesen et al. (2018).

the case of project 2013.1.00937.S, we took the information from R. K. Friesen et al. (2018).

3 RESULTS

3.1 Proper motions

The positions of SM1-A and Source X were determined by fitting a 2D Gaussian function to the images using the CASA task IMFIT. Two corrections were subsequently applied to the measured positions. The first correction accounts for changes in the catalogued positions of the gain calibrator used in each observation (see Table 1). The second correction corresponds to the trigonometric parallax. We adopted the parallax of $\varpi = 7.28 \pm 0.06$ mas, reported by G. N. Ortiz-León et al. (2017), for the Lynds 1688 star formation region, located in the ρ Ophiuchi molecular complex. In both cases, the corrections followed the same procedure as in R. Hernández-Garnica et al. (2024). Table 2 lists the positions of SM1-A and Source X before and after the application of these corrections. The positional uncertainties in right ascension and declination for both components were obtained by adding in quadrature the errors provided by IMFIT and additional systematic uncertainties, since the former are known to be underestimated (J. J. Condon 1997). The systematic terms in the positions were adjusted to obtain reduced χ^2 values close to unity for the linear fits to the proper motions. For SM1-A, we found systematic errors in right ascension of 3.3 mas in the *X* band and 1.3 mas in the *K* and *Q* bands, which are also present in the ALMA observations. In declination, the corresponding systematic errors are 55.2 mas in the *X* band and 9.2 mas in the *K* and *Q* bands, and 11.2 mas in the ALMA data. On the other hand, for Source X we found systematic errors of 1.6 mas in right ascension and 22.0 mas in declination. The fully corrected positions are shown in Fig. 2. A linear fit to these positions over time (also shown in Fig. 2) results in the proper motions for SM1-A:

$$\mu_\alpha^{SM1A} \cos\delta = -9.11 \pm 1.43 \text{ mas yr}^{-1} \quad (1)$$
$$\mu_\delta^{SM1A} = -25.49 \pm 0.92 \text{ mas yr}^{-1}, \quad (2)$$

and for Source X:

$$\mu_\alpha^{X} \cos\delta = -1.15 \pm 2.55 \text{ mas yr}^{-1} \quad (3)$$
$$\mu_\delta^{X} = -22.70 \pm 2.37 \text{ mas yr}^{-1}. \quad (4)$$

In order to compare these results with the proper motions of VLA 1623, we adopted source B as representative of the whole system. This is reasonable because VLA 1623 B is the most massive component in VLA 1623 (see S. I. Sadavoy et al. 2024) and its proper motions are similar to, and intermediate between, those of VLA 1623 A and VLA 1623 W. The astrometric analysis of VLA 1623 is presented in detail in R. Hernández-Garnica et al. (2026) and follows exactly the same calibration and analysis procedure described above for SM1-A and Source X. Therefore, only the characteristics specific to the VLA 1623 data set are summarized here. A total of 37 archival observations were selected to ensure sufficient angular resolution to resolve components A and B, which are separated by approximately 1.2 arcsec

Downloaded from academic.oup.com/mnras/article/553/1/stag1788/9006207 by guest on 09 November 2026

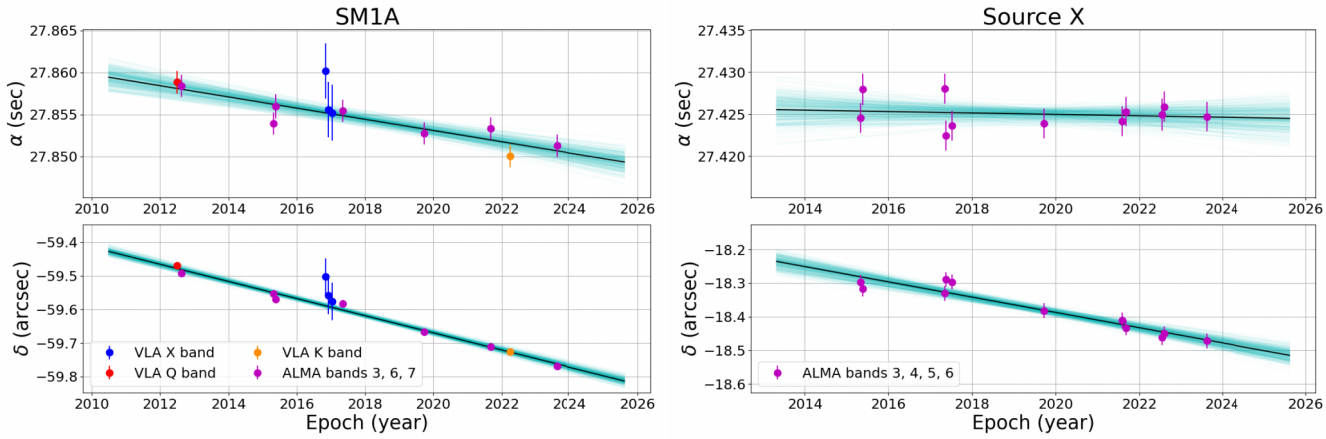


Figure 2. Left: Right ascension (top) and declination (bottom) as a function of time for SM1-A. Right: Right ascension (top) and declination (bottom) as a function of time for Source X. The different observing bands are indicated in the legends. The solid line in each panel corresponds to the best-fitting model assuming a linear, constant proper motion, while the semitransparent lines show 300 Monte Carlo realizations of the fit, sampling the range of possible values for the free parameters.

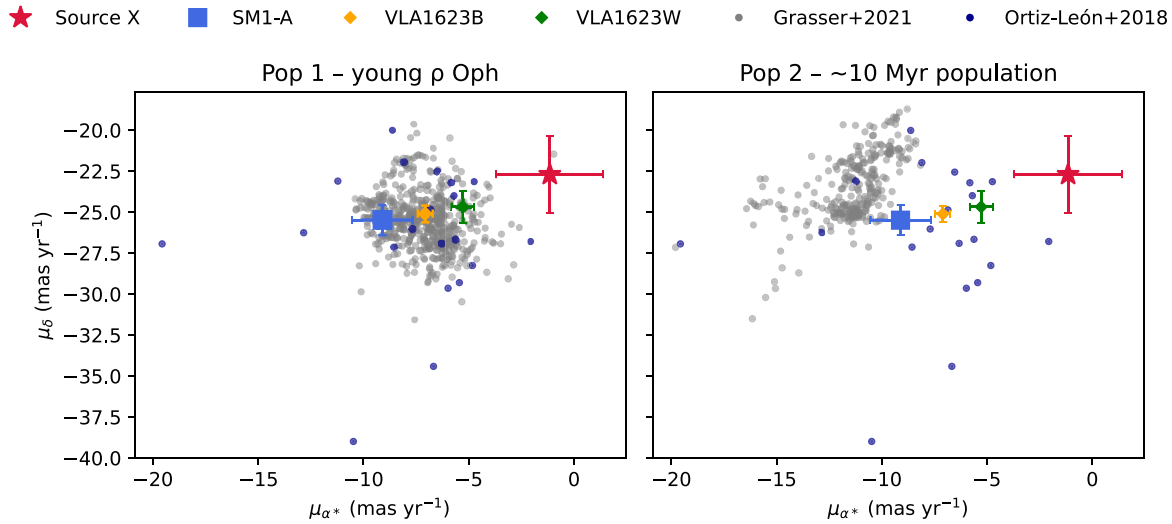


Figure 3. N. Grasser et al. (2021) proper motions of the ρ Ophiuchi region, selected to show only the high-quality ones. Left: Population 1 (youngest). Right: Population 2 (oldest, 10 Myr). While SM1-A, VLA 1623 B, and VLA 1623 W lie well within the typical proper motions of the Population 1 group, it is clear that Source X lies outside the cloud of known Ophiuchus members. For completeness, the proper motions measured by G. N. Ortiz-León et al. (2018) are also included, excluding the YLW 12Bab object, a well-known wide multiple system. It is clear that the radio-selected sample of G. N. Ortiz-León et al. (2018) primarily traces the younger population.

(D. Ward-Thompson et al. 2011). The data set comprises 16 VLA observations obtained in the *C* (∼6 GHz), *X* (∼10 GHz), *Ku* (∼15 GHz), *K* (∼22 GHz), and *Q* (∼45 GHz) bands, together with 21 ALMA observations in Bands 3 (∼100 GHz), 4 (∼150 GHz), 5 (∼190 GHz), 6 (∼230 GHz), and 7 (∼330 GHz). The resulting time baseline is approximately 34.5 yr for component B and 32.5 yr for component W. Component positions were determined by fitting 2D Gaussian functions using the CASA task `IMFIT`. As described above, the measured positions were corrected for temporal variations in the catalogued positions of the gain calibrators and for parallax, adopting $\varpi = 7.28 \pm 0.06$ mas. This value, as we mentioned before, corresponds to the mean parallax of the L1688 core measured by G. N. Ortiz-León et al. (2017), who found no evidence that the cloud is significantly more extended along the line of sight than on the plane of the sky (its projected size being ∼ 1.8 pc). Absolute proper motions were then derived by fitting a uniform linear motion to the corrected positions using the `curve_fit` routine from `scipy.optimize`. The positions of the gain calibrators were taken from the official ALMA and NRAO calibrator catalogues, whose coordinates are tied to the ICRF and have sub-milliarcsecond accuracy. Standard phase referencing was applied to all data sets. While the target was not located exactly at the phase centre in a few VLA observations, the angular offset was sufficiently small that any off-axis imaging effects or geometric distortions are expected to be negligible compared with the astrometric uncertainties. According to previous estimates (R. Hernández-Garnica et al. 2026), the proper motions for VLA 1623 A and W are:

$$\mu_\alpha^{\rm A} \cos\delta = -10.08 \pm 0.73 \text{ mas yr}^{-1} \quad (5)$$
$$\mu_\delta^{\rm A} = -25.84 \pm 1.16 \text{ mas yr}^{-1}, \quad (6)$$

Downloaded from academic.oup.com/mnras/article/553/1/stag1788/9006207 by guest on 09 November 2026

$$\mu_\alpha^{\rm W}\cos\delta = -5.28 \pm 0.54 \text{ mas yr}^{-1} \quad (7)$$
$$\mu_\delta^{\rm W} = -24.68 \pm 0.97 \text{ mas yr}^{-1}. \quad (8)$$

Additionally, source B is bright and compact in all VLA and ALMA observations, and detected over a longer time span than any other source in the system. As a result, its proper motions are particularly well determined (R. Hernández-Garnica et al. 2026):

$$\mu_\alpha^{\rm B}\cos\delta = -7.10 \pm 0.36 \text{ mas yr}^{-1} \quad (9)$$
$$\mu_\delta^{\rm B} = -25.11 \pm 0.50 \text{ mas yr}^{-1}. \quad (10)$$

A comparison of equations (1)–(10) shows that, while the proper motions of SM1-A are consistent with those of VLA 1623 B, those of Source X appear markedly different in right ascension, while in declination the values are still consistent within uncertainties, although only marginally.

In order to explore this in more detail, we have put together the available astrometric data in Ophiuchus. In Fig. 3, the proper motions for Source X, SM1-A, VLA 1623 B, and VLA 1623 W are drawn in a (μ_α–μ_δ) diagram of Ophiuchus. In this plot, we have included the VLBA data from G. N. Ortiz-León et al. (2018) and the *Gaia* data from N. Grasser et al. (2021)[1], along with our measurements reported above. We also considered the work of T. L. Esplin & K. L. Luhman (2020). However, since it is based on *Gaia* DR2 data, while N. Grasser et al. (2021) uses *Gaia* DR3 data, we decided not to include the T. L. Esplin & K. L. Luhman (2020) measurements in Fig. 3.

N. Grasser et al. (2021) have reported that the proper motions measured toward Ophiuchus present a bimodal distribution with one population (Pop. 1) associated with young stars around the ρ-Ophiuchi star and the main Ophiuchus clouds (L1688, L1689, L1709) and the other (Pop. 2) consisting of older stars (with an age of the order of $\sim$ 10 Myr). The proper motions of the second population are more dispersed, and N. Grasser et al. (2021) argue that the corresponding stars could be part of the Upper Sco group. The two panels in Fig. 3 correspond to the two populations identified by N. Grasser et al. (2021). It is clear that SM1-A, VLA 1623 B, and VLA 1623 W lie well within the typical proper motions of Pop. 1, while Source X sits outside the proper motion loci defined by the two known Ophiuchus populations in $\mu_\alpha - \mu_\delta$ space. Thus, the proper motion of Source X appears to be statistically different from the proper motions of the sources belonging to Ophiuchus: it is clearly anomalous.[2] In the rest of the paper, we will focus the discussion mainly on this object.

Fig.4 presents the trajectories of Source X and VLA 1623 W traced backwards assuming linear and uniform motions. In this figure, all positions and proper motions are referenced to VLA 1623 B (see Section 3.1). From the study of R. Hernández-Garnica et al. (2026), the proper motion of VLA 1623 W relative to B is $\Delta\mu_\alpha^{W-B} = +2.51 \pm 0.60$ mas yr^{-1}, $\Delta\mu_\delta^{W-B} = +1.00 \pm 0.79$ mas yr^{-1}. From equations (3)–(10), the relative proper motion of Source X with respect to B is $\Delta\mu_\alpha^{X-B} = +5.95 \pm 2.58$ mas yr^{-1}, $\Delta\mu_\delta^{X-B} = +2.41 \pm 2.42$ mas yr^{-1}. Note that this corresponds to a tangential velocity between Source X and B of 4.2 ± 2.3 km s^{-1}. Within the errors, the backward path of Source X encompasses an area that includes both the VLA 1623 A/B system and VLA 1623 W. Indeed, the nominal backward extrapolation indicates that the (plane of sky) closest approach between Source X and VLA 1623 W occurred 7244 yr ago, when their relative angular separation in the sky was $\sim$ 1.1 arcsec, corresponding to a projected separation of $\sim$152.8 au (orange and blue diamonds in Fig. 4). On the other hand, the error cone for Source X also includes the VLA 1623 A/B system. The (plane of sky) closest approach, in this case, occurred 2928 years ago, when their relative angular separation in the sky was $\sim$ 5.7 arcsec, corresponding to a projected separation of $\sim$784.6 au (orange star in Fig. 4). Additionally, the literature values for the systemic radial velocities of the VLA 1623 system are +3.8 km s^{-1} for the A/B components (S. Ohashi et al. 2022), and +1.6 km s^{-1} for the W component (S. Mercimek et al. 2023). However, as no radial velocity measurements are available for Source X and SM1-A, we limit our analysis to their tangential velocities. In summary, the backward extrapolations of the proper motions are consistent with Source X having been ejected from either VLA 1623 W or VLA 1623 A/B within the last $\sim$7000 yr. Note that this is less than, but of the order of, the typical lifetime (10 000–50 000 yr; I. Evans et al. 2009) of a Class 0 object, such as VLA 1623. The possibility that Source X was ejected from VLA 1623 A/B or from VLA 1623 W is explored in more detail in Section 4.

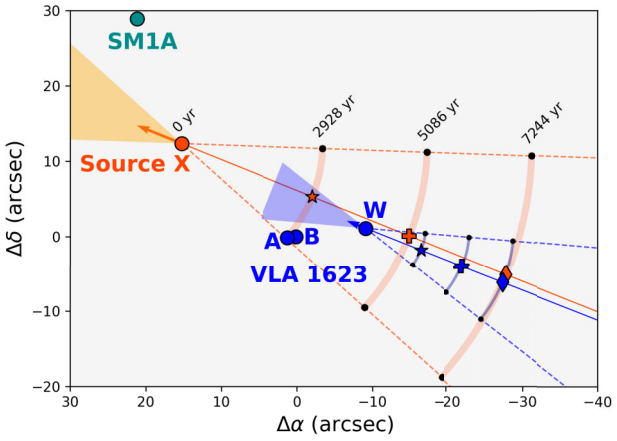


Figure 4. Sketch of the backward trajectory of Source X and VLA 1623 W, with positions and proper motions referenced to source VLA 1623 B. The cyan and orange points correspond to current positions of the sources SM1-A and Source X, respectively, while the positions of the members of VLA 1623 system are marked with blue points. The proper motions are indicated with an orange arrow in the case of Source X and a blue arrow in the case of VLA 1623 W. The blue and orange shaded cones represent the 2D projected uncertainties on the proper motions of VLA 1623 W and Source X, respectively. The dashed blue and orange cones outline the corresponding uncertainties of the backward traces. The orange star, cross, and diamond indicate the expected positions of Source X 2928, 5086, and 7244 yr ago, respectively. The blue star, cross, and diamond show the corresponding expected positions of VLA 1623 W at the same times. The closest approach between Source X and VLA 1623 A/B occurred about 2928 yr ago, while that between Source X and VLA 1623 W occurred 7244 yr ago.

[1]For the N. Grasser et al. (2021) sample, we have only represented the astrometric data with the highest quality: RUWE < 1.4, parallax > 0.0, and $e_{parallax}$/parallax < 0.1, with $e_{parallax}$ being the parallax error.
[2]The potential uncertainties introduced by an unresolved binary or disc substructure to the proper motion measurement of Source X are likely negligible because the binary would have a small separation, < 8 au, and the substructure of the disc is symmetric (see Section 3.3). The uncertainties in the proper motion of Source X most likely arise because of its weak intensity, and future observations will be crucial to reduce them and provide tighter constraints on the proper motion reported in this work.

Downloaded from academic.oup.com/mnras/article/553/1/stag1788/9006207 by guest on 09 November 2026

An obvious limitation of the analysis above is the assumption of linear and uniform proper motions. Several studies suggest that the VLA 1623 A/B and W components are gravitationally bound. For instance, the presence of streamers connecting the envelopes of the VLA 1623 A/B pair with the VLA 1623 W component (S. Mercimek et al. 2023) suggests that VLA 1623 W formed *in situ*, along with VLA 1623 A/B, through turbulent fragmentation (S. I. Sadavoy et al. 2024). This would imply that the relative motions should be elliptical (Keplerian) rather than linear and uniform. We note, however, that, in this case, the orbital period of source W would be long compared with the time of closest approach estimated earlier. S. I. Sadavoy et al. (2024) estimated masses of 0.27±0.03 $M_\odot$, $1.9^{+0.3}_{-0.2}$ $M_\odot$, and 0.64± 0.06 $M_\odot$ for components A, B, and W, respectively, so the total mass of the system can be taken to be about 3 $M_\odot$. If we assume the current separation between VLA 1623 A/B and W (about 10 arcsec $\simeq$ 1400 au) to be a good proxy for the semimajor axis, we obtain an orbital period of about 30 000 yr. This is an order of magnitude longer than the time since closest approach between Source X and W, calculated earlier, so assuming linear and uniform motions should be a reasonable approximation.

3.2 SED from ALMA + *JWST* data

In order to build the spectral energy distribution (SED) of Source X, we used the data compiled by R. Kawabe et al. (2018) in their table 3, also included in the SUbstellar CANdidates at Early Stages database (SUCANES[3]; A. M. Pérez-García et al. 2025). However, these compilations do not include any detection at wavelengths shorter than 1.3 mm (apart from the X-ray data). Therefore, we complemented with archival *JWST* images from program 2739 by PI Klaus M. Pontoppidan and program 3034 by PI Ke Zhang. The data, analyzed using the Photutils package (L. Bradley et al. 2025), reveal that both Source X and SM1-A are detected in the *F*444*W* and *F*770 *JWST* filters. Fig. 1 shows the 4.44 μm *JWST* image with the corresponding detections.

We obtained the flux density of Source X using aperture photometry. The flux was measured within a circular aperture centred on the source position, with radii of 4 and 5 pixels for the *F*444*W* and *F*770*W* filters, which have pixel scales of 0.063 and 0.111 arcsec pixel^{-1}, respectively. The local background contribution was estimated using a concentric annulus with inner and outer radii of 8 and 16 pixels for *F*444*W*, and 10 and 20 pixels for *F*770*W*, respectively, and the flux within the annulus was subtracted from the total aperture flux. As a quantitative consistency check, the aperture photometry results were compared with PSF-fitting photometry performed using the Photutils package and theoretical PSFs generated with STPSF (M. D. Perrin et al. 2012), finding agreement within the photometric uncertainties. The full table including the ALMA + VLA photometry from R. Kawabe et al. (2018) and A. M. Pérez-García et al. (2025), and the *JWST* photometry derived in this work is provided in Table A1. For completeness, Table A2 provides the *JWST* fluxes for SM1-A.

In addition, the upper limits of Source X at 24 and 70 μm (also given in Table A1) are estimated as follows. We placed empty apertures close to the position of the source and obtained the rms of the flux within the apertures, avoiding the regions with higher background gradients. We obtained a flux rms of ∼ 14 mJy at 24 μm and ∼ 230 mJy at 70 μm. We adopt 3σ upper limits for Source X of ∼ 42 mJy at 24 μm and 690 mJy at 70 μm.

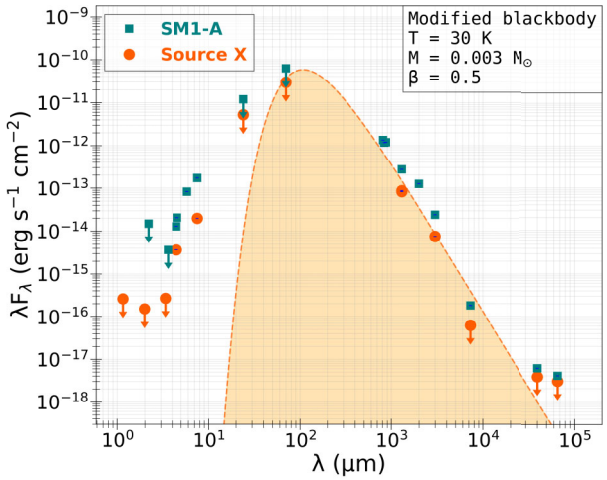


Figure 5. SED including the measurements from R. Kawabe et al. (2018), the *JWST* photometry (this work), and the upper limits from *Spitzer* and *Herschel* measured in this work for Source X (circles) and SM1-A (squares). A modified blackbody is shown as an illustrative curve that passes through the 70 μm and ALMA fluxes of Source X, and corresponds to a dust temperature of 30 K, a mass of 0.003 $M_\odot$, and a dust emissivity index of 0.5.

With the upper limit of Source X at 70 μm, an upper limit to the internal luminosity, $L_{\rm int}$ [4], can be estimated. To do this, we followed the most updated relation between $L_{\rm int}$ and the flux at 70 μm, given in equation (7) of M. M. Dunham et al. (2026), yielding $L_{\rm int} < 0.11$ $L_\odot$. Alternatively, if an object is detected in three *JWST* filters (or equivalent filters), M. M. Dunham et al. (2026) show that certain combinations are appropriate to estimate $L_{\rm int}$. By using the fluxes measured at 4.44 and 7.70 μm and the upper limit at 24 μm, and using equation 14 of M. M. Dunham et al. (2026), a value of $L_{\rm int} < 0.11$ $L_\odot$ is obtained (after applying the correction of equation 13 of M. M. Dunham et al. 2026). Thus, the two independent methods used to estimate an upper limit for $L_{\rm int}$ of Source X consistently yield $L_{\rm int} < 0.11$ $L_\odot$.

The SED for Source X is presented in Fig. 5 (orange circles). This is the first time that the *JWST* fluxes for Source X are reported. However, given the paucity of detections in the critical range from 10 μm to 1 mm, we did not attempt a formal fit to the SED. Instead, we only show in the figure, for illustrative purposes, a modified blackbody model that reproduces both the upper limit at 70 μm and the ALMA data. The modified blackbody shown in Fig. 5, calculated using a dust absorption coefficient at 1000 GHz of 0.1 g cm^{-2} (S. V. W. Beckwith et al. 1990), corresponds to a dust temperature of 30 K, a mass of gas and dust of 0.003 $M_\odot$, and a dust emissivity index of 0.5.

In Fig. 5, the SED for SM1-A is also shown. As can be seen from the figure and from Tables A1 and A2, SM1-A presents larger flux densities at all wavelengths compared to Source X. This allows to set a tighter constraint on $L_{\rm int}$ for Source X. Since R. Kawabe et al. (2018) estimate a bolometric luminosity of ∼ 0.035 $L_\odot$ for SM1-

[3]The SUCANES Database contains continuum photometry covering from optical to cm wavelengths (optical, NIR, *Spitzer*, *Herschel*, sub-mm, and cm).

[4]$L_{\rm int}$ is the total luminosity of the object excluding the contribution of the interstellar radiation field (e.g. M. M. Dunham et al. 2008). Thus, $L_{\rm int}$ must be smaller or equal to the bolometric luminosity.

Downloaded from academic.oup.com/mnras/article/553/1/stag1788/9006207 by guest on 09 November 2026

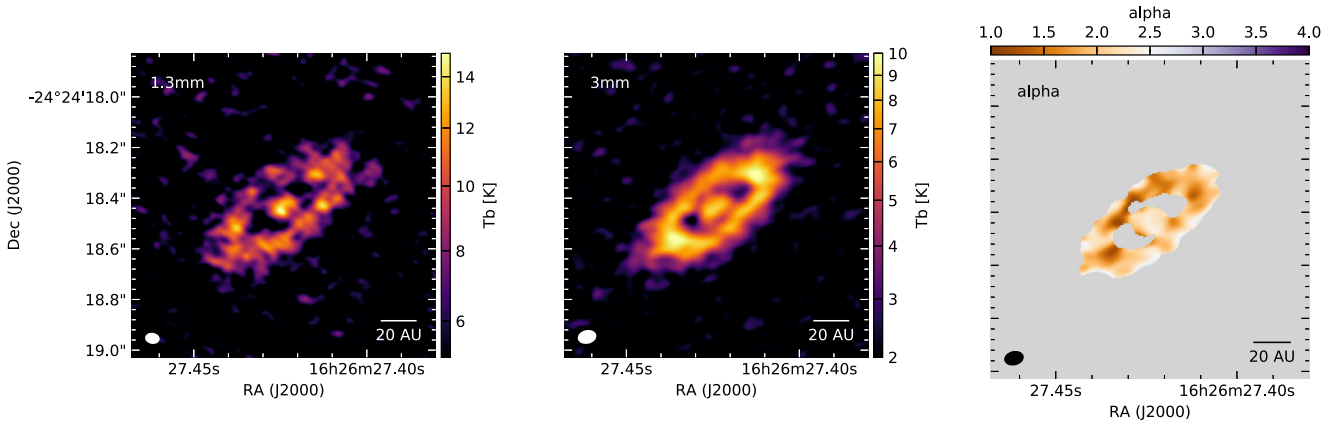


Figure 6. ALMA emission at 1.3 mm (left) and 3 mm (centre) showing the structured disc of Source X. The panel on the right corresponds to the spectral index obtained from both wavelengths, using the same *uv*-range.

A, based on the finding of an optically thick surface at 359 GHz and an estimate of the dust temperature from the SED, the bolometric luminosity and thus $L_{\rm int}$ of Source X must be smaller than 0.035 $L_\odot$. Using the relation between $L_{\rm int}$ and accreted (dynamical) mass reported by A. Palau et al. (2024) and L. Hartmann et al. (2025), the $L_{\rm int}$ upper limit of 0.035 $L_\odot$ for Source X corresponds to an accreted mass of < 0.07 $M_\odot$. Estimates of upper limits for the mass of the central object of Source X were also obtained from the *JWST* photometry and the evolutionary tracks of I. Baraffe et al. (2015) and G. Chabrier et al. (2023) and are summarized in Appendix B. However, given the large uncertainties associated with the extinction law of the ρ-Oph cloud, with $R_{\rm v}$ values for ρ-Oph ranging from 3.35 to 5.5 (e.g. B. Mookerjea et al. 2018; J. Li & X. Chen 2023), a large range of (upper limits of) masses, from 0.02 to 0.15 $M_\odot$, is obtained for Source X. Thus, for the rest of the paper, an upper limit for the accreted mass of < 0.07 $M_\odot$ is adopted.

3.3 ALMA sub-arcsecond continuum emission of Source X

The large-scale 1.3 mm ALMA emission at about 1 arcsec resolution, presented in Fig. 1, corresponds to project 2013.1.00839.S (P.I. Fumitaka Nakamura) of Table 1. It enables a first estimate of the envelope mass of SM1-A and Source X. The 1.3 mm measured flux densities of Source X and SM1-A are 39.1 and 133 mJy, respectively, corresponding to a mass of gas + dust of ~ 0.0048 $M_\odot$ for Source X and ~ 0.016 $M_\odot$ for SM1-A. These masses were obtained by assuming a dust temperature of ~ 20 K, a gas-to-dust mass ratio of 100, and a dust opacity per unit mass of dust + gas at 1.3 mm of 0.03 $\rm cm^2\ g^{-1}$ (DSHARP power-law from T. Birnstiel et al. 2018).

In order to explore the morphology and spatial distribution of the millimetre emission of Source X, we also used project 2019.1.01074.S (P.I. María José Maureira), which provides an angular resolution of $\lesssim 0.1$ arcsec at both 1.3 and 3 mm. Fig. 6 shows the ALMA image of this project at 3 and 1.3 mm, centred on Source X. As can be seen from the figure, the most striking feature revealed by these high-resolution data is a highly structured disc with a well-defined ring at both wavelengths and a compact source at the centre.

The ring-like morphology is better revealed from the intensity radial profiles (Fig. 7), which were computed from the dust continuum images using the package `GoFish` (R. Teague 2019). The inclination (i, with respect to the plane-of-sky) and position angle (PA) of the disc were estimated by fitting a Gaussian function to the disc morphology in both bands. Both fits yielded the same constraints: $i = 65$ deg and PA $= -52$ deg. From the radial profiles, we identify a ring at a de-projected radius of 32 au, and a gap at 17 au.

The flux density of the entire emission at 1.3 mm is 31.5 ± 3.2 mJy (the calibration errors in ALMA Band 3 and Band 6 are 5 and 10 per cent, respectively[5]). This flux corresponds to a disc mass of gas + dust of 0.0039 ± 0.0004 $M_\odot$, using the same assumptions as above. This is consistent with the value reported by R. K. Friesen et al. (2018) in table 2 for this source. At 3 mm, the flux density is 6.02 ± 0.30 mJy, corresponding to a mass of gas + dust of 0.033 ± 0.002 $M_\odot$ (adopting the same assumptions used at 1.3 mm, and a dust opacity per unit mass of dust + gas at 3 mm of 0.003 $\rm cm^2\ g^{-1}$, from the DSHARP power-law of T. Birnstiel et al. 2018), a factor of 2 below the 3 mm ALMA estimate by H. Kirk et al. (2017), of ~ 0.07 $M_\odot$, obtained with a more compact configuration. The difference in the estimated masses at the two wavelengths may arise from different optical depth regimes. For the rest of the paper, a gas + dust disc mass in the range 0.004–0.033 $M_\odot$, or 0.018 ± 0.014 $M_\odot$, is adopted.

The R_{90} disc radius (the radius within which 90 per cent of the total flux is enclosed) is 56.9 ± 8.9 au. This radius was estimated from the curve of growth in both Band 3 and Band 6. The fact that a similar radius is measured at both wavelengths suggests that the spatial distribution of the large particles traced at 1.3 mm is similar to that traced at 3 mm, which is consistent with the dust trap scenario and the absence of significant radial drift.

The emission morphology of Source X is particular. For example, the brightness contrast between the ring and the central region decreases from 1.3 to 3 mm, suggesting that the centre is optically thinner than the ring, in contrast to what is typically observed in protoplanetary discs around solar-mass stars (A. A. Rota et al. 2024). This property could be explained by a strong dust trap in the ring, which traps dust grains and prevents their migration towards the central star (e.g. P. Pinilla et al. 2012). Alternatively, it could be explained by the presence of dust

[5]ALMA Proposer's guide.

Downloaded from academic.oup.com/mnras/article/553/1/stag1788/9006207 by guest on 09 November 2026

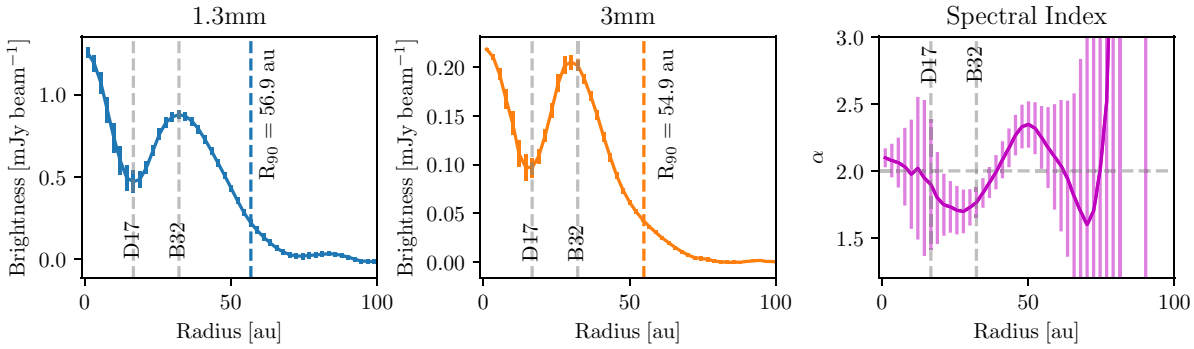


Figure 7. Brightness radial profile of Source X at ALMA Band 6 (left) and Band 3 (middle). The coloured dashed lines indicate the R_{90} disc radius. Right: Spectral index radial profile between ALMA Band 6 and 3. The horizontal dashed line at $\alpha = 2$ indicates the optically thick regime. The vertical grey dashed lines in all panels indicate the radius of the gap at 17 au (D17) and the ring at 32 au (B32).

grains with sizes up to $a \sim \lambda/2\pi = 480$ μm in the ring, which have a higher emissivity at 3 mm than at 1.3 mm (B. T. Draine 2006).

The panel on the right of Fig. 6 presents the spectral index map, obtained by aligning the 1.3 and 3 mm images based on a cross-correlation that indicated offsets smaller than 6.2 mas in RA and Dec. As can be seen from this panel, the spectral indices along the ring range from 1.5 to 2.5, being around 2.5 in the centre and ∼ 1.5 in the ring, confirming that the ring is optically thicker. The spectral index radial profile is shown in the right panel of Fig. 7, where the region around the ring presents a spectral index below 2, and it only increases to ∼ 2.3 at ∼ 50 au, indicating that most of the disc is in the optically thick regime between these bands. The very low spectral indices observed in the ring ($\alpha < 2$) can be explained by scattering from millimetre-sized dust grains in the optically thick regime, temperature gradients along the line of sight, or efficient settling of dust grains towards the midplane (A. Sierra & S. Lizano 2020).

The possible explanations of the dust properties of the ring imply a somewhat exceptional object, e.g. one with a very strong dust trap, and with a large disc-to-stellar mass ratio of $M_{\rm disc}/M_{\rm star} > 0.5$ if we consider the disc mass derived at 3 mm (less affected by dust opacity) and $M_{\rm star} < 0.07$ $M_\odot$ (Section 3.2). The origin of such a peculiar disc is further discussed in Section 5.2.

4 POSSIBLE SCENARIOS FOR THE ANOMALOUS PROPER MOTIONS OF SOURCE X

The anomalous proper motion of Source X (Fig. 3 and Section 3.1) suggests that Source X could have been ejected in a dynamical event. There are two main scenarios of ejection: dynamical interaction of three or more protostellar cores, and dynamical interaction of the fragments of a disc around a protostellar object (disc fragmentation). These scenarios are briefly discussed below.

4.1 Dynamical interaction of the VLA 1623 protostellar objects and subsequent ejection

A first possibility is that Source X results from a dynamical interaction between three or more protostellar cores, as suggested by B. Reipurth & C. Clarke (2001) and P. Kroupa & J. Bouvier (2003). Given the proximity of Source X to the VLA 1623 system and the measured proper motions, it seems feasible that the VLA 1623 system could have undergone such an event. Numerical simulations of *N*-body dynamics in dense, multiple-system environments have shown that such interactions frequently lead to the ejection of the lowest-mass members (M. R. Bate, I. A. Bonnell & V. Bromm 2002; S. P. Goodwin, A. P. Whitworth & D. Ward-Thompson 2004).

When considering a three-body ejection scenario, it usually results in a closely packed system and a clearly escaping low-mass object (e.g. J. P. Anosova 1986). The current architecture of VLA 1623 presents challenges to this interpretation, as the system harbours at least four objects in an area smaller than 1500 au. VLA 1623 W lies about 1400 au from VLA 1623 A/B and seems to be moving towards it (R. Hernández-Garnica et al. 2026), an unlikely configuration for a standard post-ejection three-body system (e.g. B. Reipurth & C. Clarke 2001). This suggests a more complex dynamical history than a single ejection driven by the interplay between gravitational scattering and gas-induced damping.

The presence of gas plays a decisive role in the outcome of these interactions, since it can exert dynamical friction on the protostars, dissipating orbital energy and potentially leading to orbital decay or the capture of members trying to escape into wide, stable orbits (M. R. Bate et al. 2002; M. R. Bate 2012). This could provide a physical mechanism to explain the behaviour of VLA 1623 W as its seemingly motion towards the central binary may suggest a future close encounter during which the presence of a dense gaseous environment is expected to soften the interaction through dynamical friction. A precedent for this outcome is found in the study of the formation of the α Centauri system, where gas drag has been shown to prevent the total ejection of a third component, stabilizing it in a wide orbit after the dynamical encounter (B. Reipurth & S. Mikkola 2012).

Nevertheless, more complex simulations of unstable systems involving more than five bodies (e.g. R. J. Allison & S. P. Goodwin 2011) show that dynamical decay can produce long-lived, wide configurations and even secondary captures before a final stable state is reached. This is consistent with the fact that the orbital time-scale of VLA 1623 W is, at most, a few times shorter than the age of the system (Section 3.1), so the system has probably only undergone a few orbits since its creation, not having reached full relaxation yet. The high multiplicity observed in such a compact area suggests that, if VLA 1623 underwent a dynamical event

Downloaded from academic.oup.com/mnras/article/553/1/stag1788/9006207 by guest on 09 November 2026

with Source X being ejected, it would require a sophisticated dynamical evolution where gas friction should play a key role in moderating the ejection of Source X while maintaining other components of the system in motion that appear inconsistent with each other. In addition, the peculiar properties of the disc associated with Source X (Section 3.3) should be explained in such a scenario. Therefore, it would be worth exploring this complex dynamical history in a future study using *N*-body or hydrodynamical simulations to fully constrain the origin and long-term stability of the system.

4.2 Disc fragmentation

4.2.1 Fragmentation of the VLA 1623 W disc

Source X could have also formed through fragmentation of a disc surrounding a protostellar object and a subsequent ejection due to dynamical interactions among the fragments of the disc (e.g. D. Stamatellos & A. P. Whitworth 2009). Since the backwards trajectory shown in Fig. 4 suggests that Source X and VLA 1623 W could have shared their position about ~ 7000 yr ago, we consider here the scenario where Source X was ejected from the VLA 1623 W disc.

VLA 1623 W has a mass of 0.66 $M_\odot$, is supposed to be a single object, and its disc radius is about 70 au (e.g. A. Michel et al. 2023). The mass of its disc has been estimated by several authors (e.g. S. Mercimek et al. 2023). Here, we take the flux density from the model of A. Michel et al. (2023), of 63 mJy, and adopt the same assumptions of Section 3.3. This yields a current disc mass of 0.026 $M_\odot$. However, since VLA 1623 W is a Class I object (e.g. N. M. Murillo & S.-P. Lai 2013), its disc mass in the past should have been larger. Following Ł. Tychoniec et al. (2020), there could be a factor of 3 decrease in disc mass from Class 0 to Class I, implying that the disc mass of VLA 1623 W could have been around 0.08 $M_\odot$ when it was in the Class 0 phase. In addition, if we consider that Source X was formed in the VLA 1623 W disc, the disc mass of VLA 1623 W before ejection should include also both the disc mass (~ 0.018 $M_\odot$, Section 3.3) and the accreted mass (< 0.07 $M_\odot$, Section 3.2) of Source X. Thus, the total disc mass of VLA 1623 W before ejection could have been close to 0.17 $M_\odot$, corresponding to a $M_{\rm disc}/M_{\rm star} \sim 0.26$, not far from the $M_{\rm disc}/M_{\rm star} \gtrsim 0.3$ required for disc fragmentation (A. Mercer & D. Stamatellos 2020; M. Teasdale & D. Stamatellos 2026a).

Typically, multiple objects form by disc fragmentation, thus, more undetected low-mass objects may exist in the region. Such objects may retain accretion discs (D. Stamatellos & A. P. Whitworth 2009; E. I. Vorobyov 2016; M. R. Bate 2018). D. Stamatellos & A. P. Whitworth (2009) find that, out of the 13 objects that are ejected in their simulations of gravitationally unstable circumstellar discs, 3 retained their discs. 2 of these 13 ejected objects are close (<1 au) low-mass binaries; both of these binaries retain their circumbinary disc. The first of these binaries has a separation of 0.3 au, components with masses 88 and 83 $M_{\rm Jup}$, and a circumbinary disc with size 30 au, and mass 8 $M_{\rm Jup}$; its ejection velocity is 0.9 km s^{-1}. The second binary has a separation of 0.6 au, components with masses 62 and 59 $M_{\rm Jup}$, and a circumbinary disc with size 10 au and mass 0.4 $M_{\rm Jup}$; its ejection velocity is 2.7 km s^{-1}. If the accreted mass estimated for Source X (< 70 $M_{\rm Jup}$, Section 3.2) was split into the two components of a binary system of equal mass, the mass of each component in Source X would be < 35 $M_{\rm Jup}$. Thus, the ejected binary systems in the simulations have masses that could be close to the Source X case. The results of these simulations demonstrate that the ejection of a low-mass binary with a disc from a fragmenting disc is possible (D. Stamatellos & A. P. Whitworth 2009). However, the $M_{\rm disc}/M_{\rm star}$ ratio of the two ejected binaries in the simulation is 0.003–0.05, well below the ratio estimated for Source X of > 0.5 (Section 3.3).

4.2.2 Fragmentation of the VLA 1623 A circumbinary disc

From the backwards trajectory shown in Fig. 4, a possible origin of Source X in VLA 1623 AB cannot be ruled out. We examine here the possibility that Source X formed in the circumbinary disc of VLA 1623 A through gravitational instability and was subsequently ejected. Such ejections are possible from circumstellar discs (D. Stamatellos et al. 2007a; D. Stamatellos & A. P. Whitworth 2009) as well as from circumbinary discs (M. Teasdale & D. Stamatellos 2024, 2026b; A. Ćalović et al. 2026; S. Nayakshin et al. 2026). In order to test this hypothesis, we used the Smooth Particle Hydrodynamics (SPH) code SEREN (D. Hubber et al. 2011) to simulate the fragmentation of gravitationally unstable circumbinary discs. Radiative processes are treated using the approximate method of J. C. Lombardi, W. G. McInally & J. A. Faber (2015), which provides a good approximation to the thermal processes within self-gravitating discs (D. Stamatellos et al. 2007b; A. Mercer, D. Stamatellos & A. Dunhill 2018; A. K. Young et al. 2024).

The total mass of the binary is well constrained, 0.27 ± 0.03 $M_\odot$ (S. I. Sadavoy et al. 2024) but the values of the other binary properties (separation, mass ratio, eccentricity) are uncertain. In our simulations, the total binary mass is set to $M_{\rm b} = 0.27\,M_\odot$, the separation to $a_{\rm b} = 30$ au, the eccentricity to $e = 0.1$, and the mass ratio to $q_{\rm b} = M_2/M_1 = 1$. The circumbinary surface density profile is set to $\Sigma \propto R^{-1}$ and its temperature profile $T \propto R^{-0.7}$, where R is the distance from the centre of mass of the binary (for details of the initial conditions see M. Teasdale & D. Stamatellos 2026a). An inner cavity of 70 au is assumed in the disc, as suggested by observations (R. J. Harris et al. 2018); typically, the cavity size is 2–3 times the binary separation, depending on the binary properties (P. Artymowicz & S. H. Lubow 1994). The disc extends out to 200 au (R. J. Harris et al. 2018). The disc mass is set to 0.13 $M_\odot$, corresponding to $M_{\rm disc}/M_{\rm star} = 0.48$, a value that allows disc fragmentation, as it is larger than the minimum value required ($M_{\rm disc}/M_{\rm star} \gtrsim 0.3$; A. Mercer & D. Stamatellos 2020). This mass corresponds to the minimum mass required for fragmentation; we also performed simulations with a disc mass of 0.12 $M_\odot$, in which the disc did not fragment.

Disc fragmentation is a stochastic process; hence, the outcome (e.g. the number and properties of the objects formed) can vary. We therefore performed an ensemble of ten simulations with different realizations of the initial disc configuration. The circumbinary discs become gravitationally unstable and fragment, producing between two and five secondary objects (a total of 36 objects), with an average of 3.6 ± 0.5 objects per disc. The simulations are terminated when 70 per cent of the disc has dissipated (i.e. accreted on to the stars of the binary or on to the secondary objects that form); this happens within $30 - 43$ kyr. Therefore, the final mass of the circumbinary disc is 0.04 $M_\odot$, which is close to the observed one (0.05 $M_\odot$; R. J. Harris et al. 2018). The masses of the objects that form by disc fragmentation in our simulations range from 5 to 46 $M_{\rm Jup}$; 64 per cent are BDs (mass > 13 $M_{\rm Jup}$), while 36 per cent are planetary-mass objects

Downloaded from academic.oup.com/mnras/article/553/1/stag1788/9006207 by guest on 09 November 2026

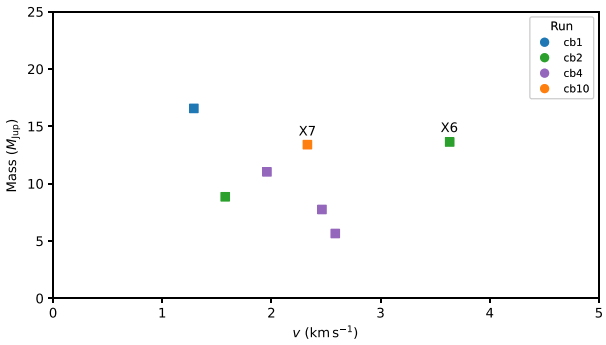


Figure 8. Numerical modelling of ejected objects from fragmenting circumbinary discs: the ejection velocity is plotted against the mass of the ejected object (for the 4 simulations, out of the 10 performed, in which there were ejected objects). Both BDs and planets are ejected. Most ejection velocities are between 1 and 3 km s^{-1}, but higher velocities are possible.

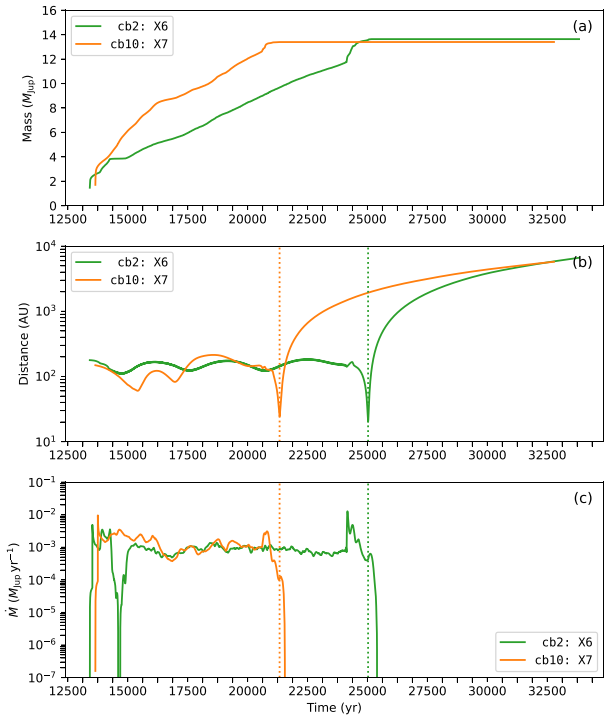


Figure 9. Two Source X analogues from the simulations: (a) mass evolution, (b) distance from the centre of mass of the binary, (c) accretion rate. Time is measured from the start of the simulation. The minima in (b) indicate the close interactions that ejected the objects (25 kyr and 21.3 kyr for X6 and X7, respectively; marked with the vertical dotted lines).

(mass < 13 M$_{Jup}$). In four simulations, objects are ejected from the disc; up to three objects are ejected per disc, with an average of 0.7 ± 0.3 ejections, corresponding to an ejection efficiency of $\sim 19 \pm 7$ per cent (7 ejected objects in total). More ejections are to be expected later on, as the resulting systems are still dynamically evolving. Approximately equal numbers of planets and BDs are ejected. The ejection velocities lie in the range 1.3–3.6 km s^{-1} (see Fig. 8). The ejected objects in these simulations do not have accretion discs (the simulations allow for the formation of such discs). However, discs may be retained depending on the detailed ejection dynamics (e.g. a milder dynamical interaction can be less violent and retain the disc more easily; D. Stamatellos & A. P. Whitworth 2009; E. I. Vorobyov 2016; M. R. Bate 2018). Previous similar simulations by D. Stamatellos & A. P. Whitworth (2009) have produced ejected objects with discs (see discussion in Section 4.2.1).

In one of the simulations, we identify two ejected objects with properties similar to those of Source X (see Fig. 9). Object X6 has a final mass of 13.6 M$_{Jup}$ and an ejection velocity of 3.6 km s^{-1}, while object X7 has a mass of 13.4 M$_{Jup}$ and an ejection velocity of 2.3 km s^{-1}. Both objects are ejected following close interactions with the binary. In general, a secondary object that forms in the disc by disc fragmentation grows rapidly while it remains embedded in the disc; the longer it stays in the disc before it is ejected, the more massive it becomes. Therefore, Source X may have spent a considerable time within the circumbinary disc if its mass is close to the estimated upper limit of ~ 70 M$_{Jup}$.

We note that, in fragmenting discs, more than one secondary object generally forms through fragmentation (D. Stamatellos & A. P. Whitworth 2009; M. Teasdale & D. Stamatellos 2026b). This is also seen in the simulations presented here. We therefore expect that additional, currently undetected objects may be associated with either the VLA 1623 A binary system or with VLA 1623 W. Such objects may have low masses and thus be difficult to detect, particularly if they do not retain circumstellar discs. It is also possible that a secondary object may have ended up on a tight orbit around one of the binary components of the VLA 1623 A binary system.

4.2.3 Object mass vs disc mass relation in the disc fragmentation scenarios

A prediction from the disc fragmentation simulations is that the ejected objects that retained their discs should present a high M_{disc}/M_{star} ratio compared to what is expected from *in situ* formation (D. Stamatellos & G. J. Herczeg 2015). In Section 3.3, we estimated the disc mass for Source X to be in the 0.004–0.033 M$_\odot$ range. As for the accreted mass or M_{star}, this was estimated to be < 0.07 M$_\odot$ (Section 3.2). Placing these numbers in the M_{disc} versus M_{star} relation from fig. 3 of D. Stamatellos & G. J. Herczeg (2015), the object seems to have an excess with respect to the relation for *in situ* collapsing prestellar cores of about two orders of magnitude (see Fig. 10). Although Source X also lies above the M_{disc}/M_{star} values expected for disc fragmentation, the excess is smaller in this last case.

Overall, we conclude that the disc fragmentation scenario can explain a number of the observed features of Source X. We favour this scenario over the dynamical interaction of protostellar objects (Section 4.1) because of the massive disc detected, closer to the outcome of the disc fragmentation simulations (although with an excess that remains to be explained) and not obviously expected in the *N*-body dynamical interaction scenario (e.g. B. Reipurth & C. Clarke 2001). However, further modelling of both scenarios exploring a wider range of (binary) parameters is required to better reproduce the observed properties of this source.

Downloaded from academic.oup.com/mnras/article/553/1/stag1788/9006207 by guest on 09 November 2026

4.3 Source X as an interloper unassociated with L1688

One alternative explanation for the anomalous proper motion of Source X is that it is an object unrelated to the L1688 molecular cloud. In this scenario, its apparent proximity to VLA 1623 and inferred close encounter with VLA 1623 W would simply result from a chance alignment along the line of sight rather than from a physical association. Although this interloper scenario cannot be ruled out with the available data, the nature of Source X remains uncertain. Its resolved dust continuum emission with a ring-like morphology, together with its infrared and X-ray counterparts, does not by themselves establish whether Source X is physically associated with the L1688 cloud or is an unrelated object projected along the same line of sight. A quantitative assessment of the interloper scenario is not straightforward, as there are currently no well-defined samples of confirmed foreground or background contaminants toward L1688 with measured proper motions that could serve as a reference population. Nevertheless, as discussed previously (Fig. 3), the proper motion of Source X is inconsistent with both the kinematics of the L1688 young stellar object population and the older stellar population identified by N. Grasser et al. (2021), which may represent foreground/background contaminants. Therefore, the currently available observational evidence does not provide conclusive support for either the interloper or the ejection scenario. Additional observations, such as independent distance estimates or radial velocity measurements, will be required to distinguish between these possibilities.

5 DISCUSSION

5.1 The nature of Source X

The nature of Source X has been debated in the literature. While the millimetre continuum emission has been detected by a number of authors (e.g. H. Kirk et al. 2017; Y.-C. Chen & N. Hirano 2018; R. K. Friesen et al. 2018; S. I. Sadavoy et al. 2019; F. Nakamura et al. 2025), the line emission is more elusive. Y.-C. Chen & N. Hirano (2018) report $C^{17}O$ (2–1) emission with the Submillimeter Array possibly associated with this source, with the peak $\sim$ 5 arcsec to the south-west and an extension towards Source X. In addition, R. Kawabe et al. (2018) report redshifted ^{12}CO (2–1) emission at the 3σ level. Since Source X is detected in X-rays, its prestellar nature is ruled out, and some authors suggest that it could be a low-mass protostellar object (e.g. R. K. Friesen et al. 2018; S. I. Sadavoy et al. 2019). However, these authors do not perform a detailed study of the SED of Source X. Given that the object had no infrared counterpart in any of the infrared surveys of the area previous to the *JWST* (e.g. see section A.26 of R. Kawabe et al. 2018; S. I. Sadavoy et al. 2019), its associated luminosity must be very low. The first work presenting a detailed study of the SED of Source X was R. Kawabe et al. (2018), who suggest a very low luminosity of $\sim$ 0.01 $L_\odot$. For this reason, these authors proposed Source X as a proto-BD candidate, and it was later included in a database of young substellar objects (SUCANES; A. M. Pérez-García et al. 2025).

The compilation of promising proto-BD candidates provided in A. Palau et al. (2024) does not include Source X. A. Palau et al. (2024) propose three main requirements for an object to be considered a good proto-BD candidate: (i) the internal luminosity, $L_{\rm int}$, must be $\leq$ 0.13 $L_\odot$ to focus on objects that likely have a substellar accreted mass (including typical uncertainties and binarity); (ii) the bolometric temperature, $T_{\rm bol}$, an evolutionary indicator, must be $<$ 650 K, to assure that the object is in the Class 0/I phase (following H. Chen et al. 1995); and (iii) the envelope mass, $M_{\rm env}$, measured with a single-dish telescope, must be $\leq$ 0.3 $M_\odot$, to assure that the mass that will be accreted in the future will not be large enough to increase the final accreted mass up to the stellar regime. A. Palau et al. (2024) applied to the entire SUCANES database the three criteria and, in Table 2 of that work, the objects from SUCANES with $L_{\rm int} < 0.13$ $L_\odot$ that do not fulfil the $T_{\rm bol}$ and/or $M_{\rm env}$ criteria are listed. As can be seen from table 2 of A. Palau et al. (2024), Source X fulfils criterion (i) and (iii). However, the T_{bol} criterion could not be assessed because the SED only had detections at wavelengths $>$ 1 mm at the time when the A. Palau et al. (2024) work was published.

With the advent of the *JWST*, Source X was detected in two different infrared filters (see Section 3.2 and F. Nakamura et al. 2025), and a preliminary estimate of $L_{\rm int}$ and $M_{\rm star}$ was performed in Section 3.2, finding that $L_{\rm int} < 0.11$ $L_\odot$ and $M_{\rm star} < 0.07$ $M_\odot$. In addition, an estimate of the total mass of gas and dust associated with Source X of $\sim$ 0.07 $M_\odot$ was obtained by H. Kirk et al. (2017), using ALMA data at 3 mm with a maximum recoverable scale of $\sim$ 20 arcsec. Since the total mass of gas + dust surrounding the object and the mass of the accreted object are similar, it is reasonable to assume that Source X must be in the Class 0/I phase, according to the criterion proposed by P. Andre, D. Ward-Thompson & M. Barsony (1993). This is consistent with the fact that the SED of Source X is a scaled-down version of the SED of

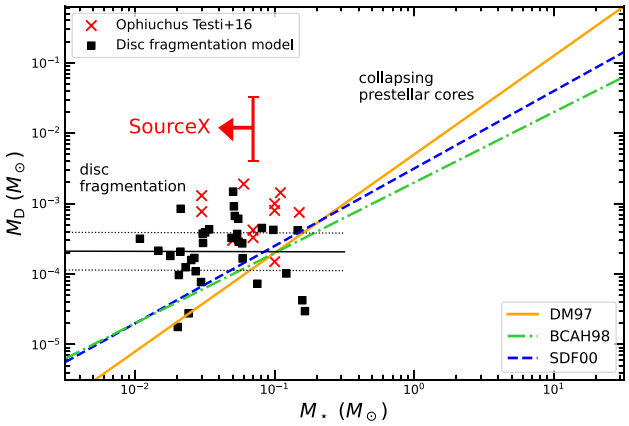


Figure 10. Updated $M_{\rm disc}$ versus $M_{\rm star}$ relation from fig. 3 of D. Stamatellos & G. J. Herczeg (2015). $M_{\rm disc}$ corresponds to the total (gas + dust) mass of the disc of the objects formed by disc fragmentation, as calculated from the hydrodynamic simulations of D. Stamatellos & A. P. Whitworth (2009), while $M_{\rm star}$ correspond to the mass of the objects hosting these discs (squares). The solid horizontal line corresponds to the best line fitted to the squares with the $\pm1\sigma$ region (dotted horizontal lines). The crosses correspond to the values of observed BD discs in Ophiuchus (L. Testi et al. 2016). The solid diagonal line and the dash-dotted diagonal lines indicate the scaling relations between $M_{\rm disc}$ and $M_{\rm star}$ from S. M. Andrews et al. (2013), based on the evolutionary models marked in the legend. This plot shows that, for $M_{\rm star} \lesssim 0.1$ $M_\odot$, the discs of objects formed through disc fragmentation have an excess in mass with respect to the discs formed through the collapse of a molecular cloud. The segment + arrow indicates the location of Source X, for which an upper limit for the accreted mass of 0.07 $M_\odot$ is estimated in Section 3.2. The estimated disc mass of Source X is 0.004–0.033 $M_\odot$ (Section 3.3), well above the expected value for discs around objects formed through the collapse of a molecular cloud, and closer to the values expected for the disc fragmentation scenario.

Downloaded from academic.oup.com/mnras/article/553/1/stag1788/9006207 by guest on 09 November 2026

SM1-A (Fig. 5), an object classified as a Class 0/I source by several authors (e.g. R. Kawabe et al. 2018; A. Palau et al. 2024; I. C. Radley et al. 2026). This, along with the fact that $L_{\rm int} < 0.11$ L$_\odot$ (this work) and $M_{\rm env} \sim 0.07$ M$_\odot$ (H. Kirk et al. 2017), strongly suggest that Source X can be classified as a good proto-BD candidate.[6]

5.2 On the origin of the massive disc with a gap in Source X

One of the most striking properties of Source X, in addition to its anomalous proper motions, is its highly substructured and massive disc hosting a prominent gap. Discs around ejected objects are somehow expected (e.g. P. J. Armitage & C. J. Clarke 1997). For example, M. R. Bate (2018) studies the properties of objects ejected from dynamical interactions in multiple systems and reports a median characteristic disc radius of 30 au at ages $< 3,000$ yr, very consistent with the radius of the ring seen in Source X, of ~ 32 au (Section 3.3). Similarly, in the disc fragmentation simulations of D. Stamatellos & A. P. Whitworth (2009), 2 out of the 13 ejected objects are BD-BD binaries and both of these retain their circumbinary discs (Section 4.2.1). Thus, from numerical work so far, it seems feasible that dynamically ejected objects retain their discs.

However, the disc detected in Source X is a peculiar one because of its well-defined, optically thick, massive ring (Section 3.3). While substructures are detected in half of the sample of the large ALMA project AGE-PRO (M. Vioque et al. 2026, the lowest mass object in their sample is 0.3 M$_\odot$), these are not so common in substellar objects. This is seen in fig. 4 of M. Vioque et al. (2026), which shows that the fraction of discs with substructures decreases from spectral types K to M5. This is because of the supposedly highly efficient radial drift in substellar objects (e.g. P. Pinilla et al. 2017). A case of a substructured disc around a young substellar object was presented recently in A. Santamaría-Miranda et al. (2025), and the substructure was indirectly inferred by fitting the visibilities in the *uv*-plane. That is, in the image plane no hints of substructure were apparent in that case. Contrary to this, the disc of Source X presents a very clear gap at ~ 17 au at both 1 and 3 mm (Section 3.3). In addition, its brightness contrast suggests that the central region is optically thinner than the ring itself (Section 3.3). The peculiar nature of the Source X disc is already appreciated in Fig. 10, where the red cross symbols correspond to BD discs in Ophiuchus (L. Testi et al. 2016). The figure shows that the mass of the Source X disc is larger than the mass of any other disc in this sample. To further show the outlier nature of the Source X disc, in Fig. 11, Source X is plotted in a size (R_{90}, radius where 90 per cent of the total continuum flux is included) versus $M_{\rm star}$ and a $M_{\rm disc}$ versus $M_{\rm star}$ diagrams, where the O. M. Guerra-Alvarado et al. (2025) sample of Lupus discs is included. The plots show that the Source X disc is the most massive and largest disc among the very low-mass objects with masses < 0.1 M$_\odot$ of Lupus. These properties make the disc around Source X a peculiar case, and could point to a dynamical origin of Source X, yielding properties different from those of discs around objects formed *in situ*.

[6]This is not the case of SM1-A, whose $M_{\rm env} \sim 4.6 > 0.3$ M$_\odot$. Thus, SM1-A does not fulfil criterion (iii) because its mass reservoir is large enough to make it a stellar object in the future (A. Palau et al. 2024).

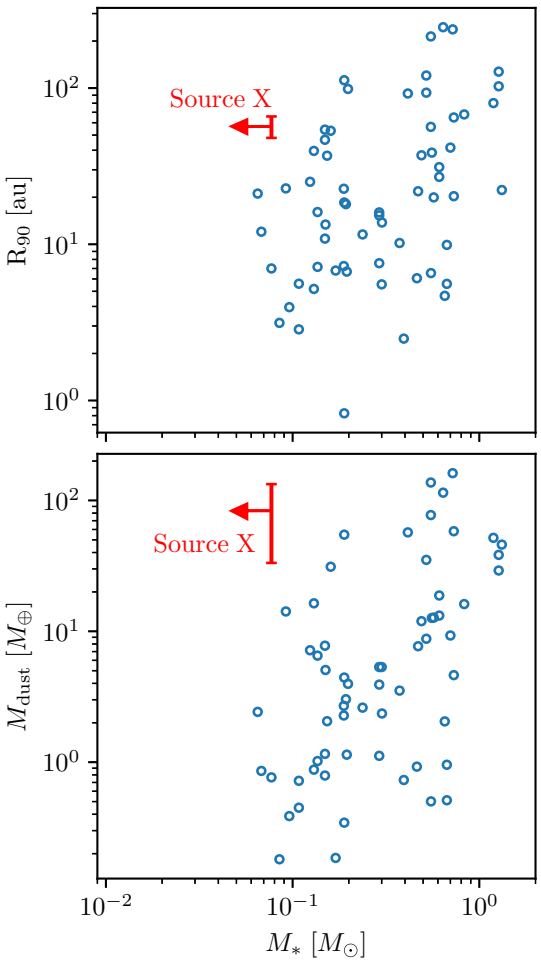


Figure 11. Top: R_{90} versus $M_{\rm star}$ relation from O. M. Guerra-Alvarado et al. (2025) of Lupus discs. Bottom: $M_{\rm dust}$ versus $M_{\rm star}$ relation from the same work. In both panels, the segment and arrow indicate the location of Source X, for which an upper limit for the accreted mass of 0.07 M$_\odot$ is adopted (Section 3.2).

Known mechanisms that naturally produce prominent cavities in discs include planets and tidal truncation by a binary system (e.g. G. A. L. Coleman, R. P. Nelson & A. H. M. J. Triaud 2022). Planets formed within the discs of proto-BDs have not been found so far, and a discussion on this possibility is completely open to the new discoveries and progress in the field. In the tidal truncation case, the gravitational pull of the companion facilitates the removal of the gas and dust in the inner parts of the disc. Typically, the cavity is about three times the semimajor axis of the binary (e.g. P. Artymowicz & S. H. Lubow 1994). In our case, this would imply a binary semimajor axis $a < 11$ au. At the distance of the system, this corresponds to an angular scale of < 0.08 arcsec, which is comparable to the angular resolution of the ALMA observations presented in Section 3.3 (0.06–0.09 arcsec). Therefore, such a binary would be difficult to resolve, particularly if it were observed near periastron. According to the disc fragmentation simulations of D. Stamatellos & A. P. Whitworth (2009), ejected objects can be BD–BD binaries, and these cases retain the discs. Thus, it would be expected that a cavity is formed in these ejected discs. However, given the separation measured in the BD-

Downloaded from academic.oup.com/mnras/article/553/1/stag1788/9006207 by guest on 09 November 2026

BD ejected objects, $\lesssim 1$ au, the expected size of the cavity should be only 3 au, about an order of magnitude smaller than what is observed in Source X.

Another mechanism to create a cavity around discs associated with objects formed *in situ* is gravitational instability (e.g. K. Kratter & G. Lodato 2016). For this to be efficient, the $M_{\rm disc}/M_{\rm star}$ ratio must be high, in the range 0.1–0.6 (e.g. K. Kratter & G. Lodato 2016; A. Mercer & D. Stamatellos 2020). For example, in the case of IRS63 (Oph-7 in the AGE-PRO sample), where gravitational instability is supposed to take place, this ratio is ~ 0.18 (D. A. Ruiz-Rodriguez et al. 2025; K. Zhang et al. 2025). For the case of Source X, $M_{\rm disc}/M_{\rm star}$ is > 0.5 if the mass at 3 mm is adopted for the disc (Section 3.3), so the disc could be gravitationally unstable and could have formed a ring by this mechanism. However, how this substellar object has formed such a massive disc, and how the gravitational instability behaves for the case of dynamically ejected objects, remains to be studied so far.

While several mechanisms could explain the formation of a prominent ring in the Source X disc, as shown in the previous paragraphs, the origin of the high disc mass is less clear. Several possibilities can be considered here. First, the disc mass as given in Section 3.3 could have been overestimated. For example, if a dust temperature of 26 K (as expected for a 0.03 $L_\odot$ object at ~ 30 au according to C. J. Chandler, M. Barsony & T. J. T. Moore 1998) instead of 20 K had been assumed, a mass range of 0.003–0.025 $M_\odot$ would be obtained, close to the 0.004–0.033 $M_\odot$ range, so this is not a big change. Alternatively, the assumed gas-to-dust mass ratio of 100 in Section 3.3 could be lower by up to one order of magnitude (~ 10, e.g. M. Ansdell et al. 2016; Y. Boehler et al. 2017; C.-J. Wu et al. 2018), yielding gas + dust masses in the range 0.0004–0.0033 $M_\odot$. However, in the recent AGE-PRO project by K. Zhang et al. (2025), who compile gas-to-dust mass ratios for different Solar Neighbourhood clouds, values from 100 up to 1000 are found for the Ophiuchus cloud, where Source X is located (see fig. 8 of K. Zhang et al. 2025). Finally, other possibilities to explain the large and massive disc around Source X include dynamical events such as capture and merger of an FFP (e.g. E. Bear, A. Kashi & N. Soker 2011), or a cloudlet capture (e.g. C. P. Dullemond et al. 2019), among others. Planet–BD mergers are supposed to have bright energetic transients and accretion discs because of tidal forces and conservation of angular momentum. On the other hand, in the cloudlet capture scenario, a low-mass cloud fragment is captured by a protostellar object, potentially contributing to its disc mass. All these scenarios are worth studying in the future.

6 CONCLUSIONS

In order to elucidate the origin of two very low luminosity objects in the VLA 1623 area, known as SM1-A and Source X, an astrometric study has been carried out using ALMA and VLA data sets. Our main conclusions can be summarized as follows:

(i) The astrometric study covers a period of 11 yr for SM1-A and 8 yr for Source X, establishing a proper motion for SM1-A in good agreement with the youngest populations in Ophiuchus, and an anomalous proper motion for Source X, which has a tangential motion of ~ 4 km s^{-1} relative to VLA 1623 B. The backward linear trajectory of Source X suggests that it was ejected from the VLA 1623 multiple system about 3000–7000 yr ago, more specifically from component W, although the possibility that the ejection originated from the A/B pair cannot be ruled out considering the uncertainties in the proper motions.

(ii) Source X is detected at 4.44 and 7.70 μm with the *JWST*, and upper limits at 24 and 70 μm were estimated. Using these measurements, an upper limit for the internal luminosity of $L_{\rm int} < 0.11$ $L_\odot$ is derived, along with an upper limit for the accreted mass of < 0.07 $M_\odot$. Taken together with the fact that the object is most likely in the Class 0/I phase, makes Source X a promising proto-BD candidate.

(iii) High angular resolution ALMA data reveal a prominent ring associated with Source X at both 1.3 and 3 mm, with a radius of ~ 32 au, and presenting a higher dust opacity than the central part of the disc. The mass of gas + dust of the disc is, assuming a gas-to-dust mass ratio of 100 and a dust temperature of 20 K, in the range 0.004–0.033 $M_\odot$.

(iv) A comparison with numerical simulations of the fragmentation of a disc around a single protostar by D. Stamatellos & A. P. Whitworth (2009), which would correspond to the fragmentation of the VLA 1623 W disc, reveals that, in these simulations, 2 out of the 13 ejected objects have properties within a factor of 2 of those of Source X: ejected velocities in the range 0.9–2.7 km s^{-1}, binarity with separations 0.3–0.6 au, binary components with masses in the range 59–88 $M_{\rm Jup}$, and disc sizes in the range 10–30 au. However, the $M_{\rm disc}/M_{\rm star}$ ratios for the ejected binaries in the simulation are much lower than the ratio of the Source X disc obtained using the disc mass from the 3 mm measurement, which is > 0.5.

(v) Numerical simulations of the disc fragmentation scenario for the circumbinary case, run specifically for the VLA 1623 A binary system, produce 2 (out of 36) ejected objects with velocities in the range 2.3–3.6 km s^{-1} and masses of ~ 14 $M_{\rm Jup}$, although none of them are binaries and none retain their disc, something which needs to be further explored.

(vi) The disc mass of Source X presents a clear excess in the $M_{\rm disc}$ versus $M_{\rm star}$ diagram, when compared to the expected trend for discs formed *in situ*, and is closer to the predictions from the disc fragmentation scenario. Whether the ejected object can retain a disc with a prominent ring is something that remains to be explored so far.

Overall, the astrometric analysis presented here suggests that the proto-BD candidate Source X has proper motions consistent with being ejected from the VLA 1623 system, prompting further observations confirming this scenario and further searches for these kinds of objects, which are crucial to test the disc fragmentation scenario for BD and FFP formation from the observational side. Furthermore, the prominent ring detected in the Source X disc calls for further modeling of substructure formation in protoplanetary discs around very low-mass objects. To progress in this direction, further observations to constrain more tightly the proper motions of Source X, and to gain insight into the nature of its infrared and X-rays emission would be highly valuable. This would allow to constrain more tightly the accreted mass of Source X. Additionally, new deep observations at wavelengths where the dust is optically thinner would allow to better constrain its $M_{\rm disc}/M_{\rm star}$ ratio, a clue parameter to understand disc and planet formation. From the numerical side, new simulations revealing the substructure of discs of ejected objects would be

Downloaded from academic.oup.com/mnras/article/553/1/stag1788/9006207 by guest on 09 November 2026

extremely useful, along with simulations of the detailed evolution of discs influenced or generated by captures of objects as the ejected object travels. These follow-up studies are vital to provide definite clues on the origin of this exceptional object.

ACKNOWLEDGEMENTS

The authors are deeply grateful to the anonymous referee, whose suggestions and comments improved the quality and clarity of this paper. AP and NH are grateful to Giovanni Miniutti and Ian Evans from the Chandra X-ray Center for their support with the Chandra image processing. This work made use of dedicated computing resources developed and maintained by the IRyA's Computing Department. The authors gratefully acknowledge the contributions of Daniel Díaz-González, Miguel Espejel, Alfonso Ginori González, and Gilberto Zavala. This paper makes use of the following ALMA data: ADS/JAO.ALMA#2011.0.00396.S, 2013.1.00839.S, 2013.1.00937.S, 2016.1.01468.S, 2015.1.01112.S, 2018.1.01205.L, 2019.1.01074.S, 2018.1.00769.S, 2022.1.01734.S. ALMA is a partnership of ESO (representing its member states), National Science Foundation (NSF, USA), and National Institutes of Natural Sciences (NINS, Japan), together with National Research Council (NRC, Canada), National Science and Technology Council (NSTC) and Academia Sinica Institute of Astronomy and Astrophysics (ASIAA, Taiwan), and Korea Astronomy and Space Science Institute (KASI, Republic of Korea), in cooperation with the Republic of Chile. The Joint ALMA Observatory is operated by ESO, AUI/NRAO, and NAOJ. The National Radio Astronomy Observatory is a facility of the U.S. National Science Foundation operated under cooperative agreement by Associated Universities, Inc. RHG acknowledges the Secretaría de Ciencia, Humanidades, Tecnología e Innovación (SECIHTI) for grant 835136. AP acknowledges financial support from the Universidad Nacional Autónoma de México (UNAM) through the Programa de Apoyo a Proyectos de Investigación e Innovación Tecnológica (PAPIIT) IN120226 grant and the Sistema Nacional de Investigadores of SECIHTI, México. LL acknowledges the support of Dirección General de Asuntos del Personal Académico (DGAPA) of UNAM grants IN108324 and IN112820, CONACyT-CF grant 263356, and SECIHTI grant CBF-2025-I-109. NH is funded by grant PID2023-150468NB-I00 by the Spain Ministry of Science and Innovation/State Agency of Research MCIN/AEI/ 10.13039/501100011033. This work has made use of the SUCANES database, a joint project funded by European Space Agency (ESA) Faculty under contract No. 4000129603/19/ES/CM, ISDEFE and CSIC. This research has made use of the SVO Filter Profile Service 'Carlos Rodrigo', funded by the Ministerio de Ciencia e Innovación (MCIN)/ Agencia Estatal de Investigación (AEI)/10.13039/501100011033/ through grant PID2023-146210NB-I00. This research has made use of data from the Herschel Gould Belt survey (HGBS) project (http://gouldbelt-herschel.cea.fr). The HGBS is a Herschel Key Programme jointly carried out by SPIRE Specialist Astronomy Group 3 (SAG 3), scientists of several institutes in the PACS Consortium (CEA Saclay, INAF-IFSI Rome and INAF-Arcetri, KU Leuven, MPIA Heidelberg), and scientists of the Herschel Science Center (HSC). CRZ acknowledges support from project UNAM-DGAPA-PAPIIT IN107226. DS acknowledges support from the COST Action CA22133:PLANETS and the Science and Technology Facilities Council (STFC) grant ST/Y002741/1. SPH simulations were performed using the University of Lancashire's High Throughput Computing (HTC) facilities, and the Cambridge Service for Data Driven Discovery (CSD3) operated by the University of Cambridge Research Computing Service (www.csd3.cam.ac.uk), provided by Dell EMC and Intel using Tier-2 funding from the Engineering and Physical Sciences Research Council (capital grant EP/T022159/1), and DiRAC funding from the Science and Technology Facilities Council (www.dirac.ac.uk). RFM thanks SECIHTI (Mexico) for a postdoc fellowship. DAVT acknowledges the SECIHTI for grant 4016700. CCG acknowledges support from DGAPA-PAPIIT project IG101224.

DATA AVAILABILITY

Data will be shared upon request to the authors.

REFERENCES

Ahmad A. A., Commerçon B., Chabrier G., Borderies A., 2025, ApJ, 991, L32
Akiyama E., Vorobyov E. I., Liu H. B., Dong R., de Leon J., Liu S.-Y., Tamura M., 2019, AJ, 157, 165
Allison R. J., Goodwin S. P., 2011, MNRAS, 415, 1967
Andre P., Ward-Thompson D., Barsony M., 1993, ApJ, 406, 122
André P. et al., 2010, A&A, 518, L102
Andrews S. M., Rosenfeld K. A., Kraus A. L., Wilner D. J., 2013, ApJ, 771, 129
Anosova J. P., 1986, Ap&SS, 124, 217
Ansdell M. et al., 2016, ApJ, 828, 46
Armitage P. J., Clarke C. J., 1997, MNRAS, 285, 540
Artymowicz P., Lubow S. H., 1994, ApJ, 421, 651
Arzoumanian D. et al., 2019, A&A, 621, A42
Baraffe I., Homeier D., Allard F., Chabrier G., 2015, A&A, 577, A42
Bate M. R., 2009, MNRAS, 392, 590
Bate M. R., 2012, MNRAS, 419, 3115
Bate M. R., 2018, MNRAS, 475, 5618
Bate M. R., 2019, MNRAS, 484, 2341
Bate M. R., Bonnell I. A., 2005, MNRAS, 356, 1201
Bate M. R., Bonnell I. A., Bromm V., 2002, MNRAS, 332, L65
Bear E., Kashi A., Soker N., 2011, MNRAS, 416, 1965
Beckwith S. V. W., Sargent A. I., Chini R. S., Guesten R., 1990, AJ, 99, 924
Bhaskar H. G., Perets H. B., 2025, ApJ, 991, 132
Birnstiel T. et al., 2018, ApJ, 869, L45
Boehler Y., Weaver E., Isella A., Ricci L., Grady C., Carpenter J., Perez L., 2017, ApJ, 840, 60
Bohlin R. C., Savage B. D., Drake J. F., 1978, ApJ, 224, 132
Boudreault S., Bailer-Jones C. A. L., 2009, ApJ, 706, 1484
Bouy H., Brandner W., Martín E. L., Delfosse X., Allard F., Basri G., 2003, AJ, 126, 1526
Bradley L. et al., 2025, astropy/photutils: 2.3.0, Zenodo, 10.5281/zenodo.17129028
Burgasser A. J., Kirkpatrick J. D., Reid I. N., Brown M. E., Miskey C. L., Gizis J. E., 2003, ApJ, 586, 512
Ćalović A., Nayakshin S., Casewell S., Miret-Roig N., 2026, MNRAS, 545, staf2097
Chabrier G., 2005, in Corbelli E., Palla F., Zinnecker H. eds, Astrophysics and Space Science Library, Vol. 327, The Initial Mass Function 50 Years Later. Springer-Verlag, Berlin, p. 41
Chabrier G., Lenoble R., 2023, ApJ, 944, L33
Chabrier G., Baraffe I., Phillips M., Debras F., 2023, A&A, 671, A119
Chandler C. J., Barsony M., Moore T. J. T., 1998, MNRAS, 299, 789
Chen H., Myers P. C., Ladd E. F., Wood D. O. S., 1995, ApJ, 445, 377
Chen Y.-C., Hirano N., 2018, ApJ, 868, 80
Close L. M., Siegler N., Freed M., Biller B., 2003, ApJ, 587, 407
Coleman G. A. L., Nelson R. P., Triaud A. H. M. J., 2022, MNRAS, 513, 2563
Condon J. J., 1997, PASP, 109, 166
Dong S. et al., 2025, Science, 391, 96

Downloaded from academic.oup.com/mnras/article/553/1/stag1788/9006207 by guest on 09 November 2026

Draine B. T., 2006, ApJ, 636, 1114
Dullemond C. P., Küffmeier M., Goicovic F., Fukagawa M., Oehl V., Kramer M., 2019, A&A, 628, A20
Dunham M. M., Crapsi A., Evans Neal J. I., Bourke T. L., Huard T. L., Myers P. C., Kauffmann J., 2008, ApJS, 179, 249
Dunham M. M., Palau A., Huélamo N., Vorobyov E. I., Yek Z., Rand S., 2026, MNRAS, 548, stag685
Esplin T. L., Luhman K. L., 2020, AJ, 159, 282
Evans Neal J. I. et al., 2009, ApJS, 181, 321
Friesen R. K., Pon A., Bourke T. L., Caselli P., Di Francesco J., Jørgensen J. K., Pineda J. E., 2018, ApJ, 869, 158
Goodwin S. P., Whitworth A. P., Ward-Thompson D., 2004, A&A, 414, 633
Grasser N. et al., 2021, A&A, 652, A2
Guerra-Alvarado O. M., van der Marel N., Williams J. P., Pinilla P., Mulders G. D., Lambrechts M., Sanchez M., 2025, A&A, 696, A232
Guo K., Ida S., Ogihara M., 2026, ApJ, 997, 34
Hadden S., Wu Y., 2026, ApJ, 1003, 70
Harris R. J. et al., 2018, ApJ, 861, 91
Hartmann L., Tobin J. J., Sheehan P., Kounkel M., Zhao C., 2025, MNRAS, 541, 4025
Haugbølle T., Padoan P., Nordlund Å., 2018, ApJ, 854, 35
Hernández-Garnica R. et al., 2024, MNRAS, 535, 2948
Hernández-Garnica R. et al., 2026, MNRAS, 551, stag1411
Hubber D. et al., 2011, SEREN: A SPH code for star and planet formation-simulations, Astrophysics Source Code Library, record ascl:1102.010
Kawabe R. et al., 2018, ApJ, 866, 141
Kirk H. et al., 2017, ApJ, 838, 114
Könyves V. et al., 2015, A&A, 584, A91
Kratter K., Lodato G., 2016, ARA&A, 54, 271
Kroupa P., Bouvier J., 2003, MNRAS, 346, 369
Kroupa P., Weidner C., Pflamm-Altenburg J., Thies I., Dabringhausen J., Marks M., Maschberger T., 2013, in Oswalt T. D., Gilmore G. eds, Planets, Stars and Stellar Systems Vol. 5, Galactic Structure and Stellar Populations. Springer, Dordrecht, p. 115
Kumar M. S. N., Schmeja S., 2007, A&A, 471, L33
Ladjelate B. et al., 2020, A&A, 638, A74
Li J., Chen X., 2023, Universe, 9, 364
Lombardi J. C., McInally W. G., Faber J. A., 2015, MNRAS, 447, 25
Madhusudhan N., Agúndez M., Moses J. I., Hu Y., 2016, Space Sci. Rev., 205, 285
McMullin J., Waters B., Schiebel D., Young W., Golap K., 2007, in Shaw R. A., Hill F., Bell D. J., eds, ASP Conf. Ser., Vol. 376, Astronomical Data Analysis Software and Systems XVI. Astron. Soc. Pac., San Francisco, p. 127
Mercer A., Stamatellos D., 2020, A&A, 633, A116
Mercer A., Stamatellos D., Dunhill A., 2018, MNRAS, 478, 3478
Mercimek S. et al., 2023, MNRAS, 522, 2384
Michel A., Sadavoy S. I., Sheehan P. D., Looney L. W., Cox E. G., Tobin J. J., van der Marel N., Segura-Cox D. M., 2023, AJ, 166, 184
Miret-Roig N. et al., 2022, Nat. Astron., 6, 89
Mookerjea B., Sandell G., Vacca W., Chambers E., Güsten R., 2018, A&A, 616, A31
Murillo N. M., Lai S.-P., 2013, ApJ, 764, L15
Nakamura F. et al., 2025, ApJ, 994, 225
Nayakshin S., Zhang L., Ćalović A., Lee H., Baruteau C., Meru F., Mayer L., 2026, MNRAS, 546, stag043
Ohashi S. et al., 2022, ApJ, 927, 54
Ortiz-León G. N. et al., 2017, ApJ, 834, 141
Ortiz-León G. N. et al., 2018, ApJ, 869, L33
Palau A., Huélamo N., Barrado D., Dunham M. M., Lee C. W., 2024, New Astron. Rev., 99, 101711
Pérez-García A. M. et al., 2025, A&A, 695, A13
Perley R. A., Chandler C. J., Butler B. J., Wrobel J. M., 2011, ApJ, 739, L1
Perrin M. D., Soummer R., Elliott E. M., Lallo M. D., Sivaramakrishnan A., 2012, in Clampin M. C., Fazio G. G., MacEwen H. A., Oschmann J. M. Jr., eds, Proc. SPIE Conf. Ser. Vol. 8442, Space Telescopes and Instrumentation 2012: Optical, Infrared, and Millimeter Wave, SPIE, Bellingham, p. 11 10.1117/12.925230
Pinilla P., Birnstiel T., Ricci L., Dullemond C. P., Uribe A. L., Testi L., Natta A., 2012, A&A, 538, A114
Pinilla P. et al., 2017, ApJ, 846, 70
Radley I. C. et al., 2026, AJ, 172, 190
Reipurth B., Clarke C., 2001, AJ, 122, 432
Reipurth B., Mikkola S., 2012, Nature, 492, 221
Reipurth B., Mikkola S., 2015, AJ, 149, 145
Reipurth B. et al., 2023, AJ, 165, 209
Rieke G. H., Lebofsky M. J., 1985, ApJ, 288, 618
Rodrigo C., Solano E., 2020, in XIV.0 Scientific Meeting (virtual) of the Spanish Astronomical Society. Spanish Astronomical Society, Spain, 182
Rodrigo C., Solano E., Bayo A., 2012, SVO Filter Profile Service Version1.0, International Virtual Observatory Alliance, Online, IVOA Working Draft 15 October 2012 Spanish Astronomical Society, Spain
Rodrigo C. et al., 2024, A&A, 689, A93
Rota A. A., Meijerhof J. D., van der Marel N., Francis L., van der Tak F. F. S., Sellek A. D., 2024, A&A, 684, A134
Roy A. et al., 2014, A&A, 562, A138
Ruiz-Rodriguez D. A. et al., 2025, ApJ, 989, 2
Sadavoy S. I. et al., 2019, ApJS, 245, 2
Sadavoy S. I. et al., 2024, A&A, 687, A308
Santamaría-Miranda A. et al., 2025, ApJ, 986, L11
Schib O., Mordasini C., Emsenhuber A., Helled R., 2025, A&A, 704, A28
Sierra A., Lizano S., 2020, ApJ, 892, 136
Stamatellos D., Herczeg G. J., 2015, MNRAS, 449, 3432
Stamatellos D., Whitworth A. P., 2009, MNRAS, 392, 413
Stamatellos D., Hubber D. A., Whitworth A. P., 2007a, MNRAS, 382, L30
Stamatellos D., Whitworth A. P., Bisbas T., Goodwin S., 2007b, A&A, 475, 37
Teague R., 2019, J. Open Source Softw., 4, 1632
Teasdale M., Stamatellos D., 2024, MNRAS, 533, 2294
Teasdale M., Stamatellos D., 2026a, MNRAS, 545, staf2129
Teasdale M., Stamatellos D., 2026b, MNRAS, 548, stag476
Testi L., Natta A., Scholz A., Tazzari M., Ricci L., de Gregorio Monsalvo I., 2016, A&A, 593, A111
Thies I., Pflamm-Altenburg J., Kroupa P., Marks M., 2015, ApJ, 800, 72
Tychoniec Ł. et al., 2020, A&A, 640, A19
Vioque M. et al., 2026, A&A, 705, A238
Vorobyov E. I., 2016, A&A, 590, A115
Ward-Thompson D., Kirk J. M., Greaves J. S., André P., 2011, MNRAS, 415, 2812
Wu C.-J., Hirano N., Takakuwa S., Yen H.-W., Aso Y., 2018, ApJ, 869, 59
Yip A. K. P., Kurtev R., Pinfield D. J., Marocco F., Gromadzki M., Carballo-Bello J. A., 2023, MNRAS, 522, 1669
Young A. K., Celeste M., Booth R. A., Rice K., Koval A., Carter E., Stamatellos D., 2024, MNRAS, 531, 1746
Zhang K. et al., 2025, ApJ, 989, 1

APPENDIX A: *JWST* PHOTOMETRY FOR SOURCE X AND SM1-A

In this Appendix, we provide tables with the flux densities used to build the SEDs for both SM1-A and Source X, described in Section 3.2.

Downloaded from academic.oup.com/mnras/article/553/1/stag1788/9006207 by guest on 09 November 2026

Table A1. Photometry for Source X.

λ (μm)	S_ν^a (mJy)	σ (mJy)	Angular resolution[b] (arcsec)	Instrument
1.154	< 0.0001	...	0.040	*JWST*/NIRCam
1.990	< 0.0001	...	0.066	*JWST*/NIRCam
3.365	< 0.0003	...	0.111	*JWST*/NIRCam
4.44	0.0054	0.0005	0.145	*JWST*/NIRCam
7.70	0.050	0.005	0.269	*JWST*/MIRI
24	< 42	...	6	*Spitzer*/MIPS
70	< 690	...	5.86	*Herschel*/PACS
1300	36.0	0.78	0.6 × 0.34	ALMA/B6
1300	37.9	1.1	1.4 × 0.92	ALMA/B6
3000	7.56	0.86	3.5 × 1.8	ALMA/B3
7300	< 0.152	...	0.32 × 0.15	JVLA
40 000	< 0.051	...	1.24 × 0.66	JVLA
66 000	< 0.066	...	2.0 × 1.0	JVLA

Notes.[a] Flux density measured at each wavelength. The fluxes at 4.44 and 7.70 μm are measured in this work as described in Section 3.2. The upper limits for *JWST*, *Spitzer*, and *Herschel* correspond to 3 times the standard deviation of the flux density measured in empty apertures around the source (Section 3.2); the upper limits for the VLA are taken from R. Kawabe et al. (2018).
[b] Empirical FWHM reported in the *JWST* documentation (https://jwst-docs.stsci.edu/jwst-near-infrared-camera/nircam-performance/nircam-point-spread-functions) and PSF FWHM for *Spitzer*. Beam size for ALMA and VLA. Some of the values are taken from R. Kawabe et al. (2018).

Table A2. Photometry for SM1-A.

λ (μm)	S_ν^a (mJy)	σ (mJy)	Angular resolution[b] (arcsec)	Instrument
2.2	< 0.011	...	0.5	IRTF/SIRIUS
3.5	< 0.0044	...	1.66	*Spitzer*/IRAC
4.44	0.088	0.007	0.145	*JWST*/NIRCam
4.5	0.31	0.01	1.72	*Spitzer*/IRAC
5.8	0.16	0.05	1.88	*Spitzer*/IRAC
7.70	0.432	0.022	0.269	*JWST*/MIRI
8.0	< 0.31	...	1.98	*Spitzer*/IRAC
24	< 96	...	6	*Spitzer*/MIPS
70	< 1460	...	5.86	*Herschel*/PACS
810	366	4.6	0.59 × 0.42	ALMA/B7
835	327	1.4	0.64 × 0.46	ALMA/B7
870	350	10	2.8 × 0.9	SMA
1300	118.3	2.0	1.4 × 0.92	ALMA/B6
2000	84	24	5.2 × 13.4	NMA
3000	24	1.8	6.2 × 3.2	NMA
7300	0.608	0.065	0.32 × 0.15	JVLA
40 000	0.125	0.056	1.24 × 0.66	JVLA
66 000	0.101	0.046	2.0 × 1.0	JVLA

Notes. [a] Flux density measured at each wavelength taken from R. Kawabe et al. (2018). The fluxes at 4.44 and 7.70 μm are measured in this work as described in Section 3.2. The upper limits are taken from R. Kawabe et al. (2018), except for the upper limit at 24 μm, which was re-measured in this work following the method of R. Kawabe et al. (2018).
[b] Empirical FWHM reported in the *JWST* documentation (https://jwst-docs.stsci.edu/jwst-near-infrared-camera/nircam-performance/nircam-point-spread-functions) and PSF FWHM for *Spitzer*, *Herschel,* and IRTF. Beam size for ALMA, NMA, SMA, and VLA. Some of the values are taken from R. Kawabe et al. (2018).

APPENDIX B: MASS ESTIMATES FOR SOURCE X FROM EVOLUTIONARY TRACKS AND *JWST* PHOTOMETRY

In order to roughly estimate the mass of the central object, the *JWST* detection at 4.44 μm was used along with the evolutionary tracks of G. Chabrier et al. (2023). The *JWST* flux at 4.44 μm reported in Table A1 was converted to 18.9 mag using the Spanish Virtual Observatory Filter Profile Service (C. Rodrigo, E. Solano & A. Bayo 2012; C. Rodrigo & E. Solano 2020; C. Rodrigo et al. 2024). This magnitude was dereddened by estimating the visual extinction along the line of sight from the Herschel Gould Belt Survey (P. André et al. 2010; A. Roy et al. 2014; D. Arzoumanian et al. 2019; B. Ladjelate et al. 2020) column density map of L1688. From this map, a H_2 column density of 1.7×10^{23} cm^{-2} was measured at the position of Source X, corresponding to a visual extinction of 181 mag following the relation $N(H_2) = 0.94 \times 10^{21} A_v$, where $N(H_2)$ is given in cm^{-2} (e.g. R. C. Bohlin, B. D. Savage & J. F. Drake 1978; V. Könyves et al. 2015). This visual extinction corresponds to an extinction of 6.3 mag at 4.4 μm, following G. H. Rieke & M. J. Lebofsky (1985). Thus, the dereddened magnitude at 4.44 μm is 12.6 mag. Assuming a distance to the source of 137.3 pc, the absolute magnitude at 4.44 μm is 6.8 mag, corresponding to 20 M_{Jup} at 1 Myr for the evolutionary tracks of G. Chabrier et al. (2023). Since these tracks are only valid for T_{eff} <2000 K, we repeated the calculation using the evolutionary models from I. Baraffe et al. (2015), obtaining consistent results. In principle, this mass estimate of ∼ 20 M_{Jup} for the central object of Source X should be regarded as an upper limit because the flux at 4.44 μm is most likely affected by the contribution of the disc. However, it is important to keep in mind that the extinction law adopted is highly uncertain for this region. While we have used G. H. Rieke & M. J. Lebofsky (1985), corresponding to a total-to-selective extinction $R_v = 3.09$, other works estimate R_v values for ρ-Oph ranging from 3.35 to 5.5 (e.g. B. Mookerjea et al. 2018; J. Li & X. Chen 2023). If a value of $R_v = 5.5$ is used, the upper limit for the accreted mass using the 3.35 μm photometry increases to 0.15 $M_\odot$. Therefore, given the large uncertainties associated with the extinction law in this region, we refrain from estimating the mass of the central object using the *JWST* photometry.

This paper has been typeset from a TEX/LATEX file prepared by the author.

Downloaded from academic.oup.com/mnras/article/553/1/stag1788/9006207 by guest on 09 November 2026

© The Author(s) 2026.
Published by Oxford University Press on behalf of Royal Astronomical Society. This is an Open Access article distributed under the terms of the Creative Commons Attribution License (https://creativecommons.org/licenses/by/4.0/), which permits unrestricted reuse, distribution, and reproduction in any medium, provided the original work is properly cited.